





Seismic Retrofitting of Existing Steel Frames with External BRBs: Pseudo-Dynamic Hybrid Testing and Numerical Parametric Analysis

Fabio Freddi ¹ 🗓 Jing-Ren Wu² Massimo Cicia ³ 🗓 Luigi Di Sarno ^{3,4} Mario D'Aniello ³ 🗓		
Fernando Gutiérrez-Urzúa ¹ 🕞 Raffaele Landolfo³ 🕒 Oh-Sung Kwon⁵ 🕞 Stathis Bousias⁶	Jamin Park ⁷ 🕩	
Nikolaos Stathas ⁶ Elias Strepelias ⁶		

Correspondence: Fabio Freddi (f.freddi@ucl.ac.uk)

Received: 28 June 2024 | Revised: 31 October 2024 | Accepted: 5 December 2024

Funding: This research was supported by the Seismic Engineering Research Infrastructure (SERA) for the "HybrId Testing of an Existing Steel Frame with Infills under Multiple Earthquakes" (HITFRAMES) SERA Project, funded within the H2020-INFRAIA-2016-2017 Framework Program of the European Commission under grant agreement No. 730900.

Keywords: buckling-restrained braces | existing steel frames | numerical parametric analysis | pseudo-dynamic hybrid testing | seismic performance | seismic retrofitting

ABSTRACT

The use of buckling-restrained braces (BRBs) is an effective strategy for improving the seismic performance of existing structures. BRBs can be included within existing frames, creating an additional load path and contributing to their strength, stiffness, ductility, and, in turn, energy dissipation capacity. However, BRBs are typically inserted within the structural mesh of the existing frames, thus requiring the demolition and reconstruction of non-structural components. The present study explores the seismic retrofitting of existing steel structures, considering an external placement of BRBs to minimize the invasiveness of the intervention scheme and, consequently, business interruptions and indirect losses. A two-story steel moment-resisting frame (MRF) designed primarily for gravity loads and retrofitted with BRBs placed externally to the frames were considered for case study purposes. The research includes large-scale Pseudo-Dynamic Hybrid tests performed as part of the HITFRAMES (i.e., HybrId Testing of an Existing Steel Frame with Infills under Multiple EarthquakeS) project funded by the EU-H2020 SERA Consortium in Europe. The experimental results provided significant insights into the seismic response of the retrofitted structure and allowed the calibration of advanced 3D finite element models. An extensive numerical parametric analysis was performed to investigate some of the key variables affecting the local and global response of the structure. The results provide valuable insights into effectively implementing this retrofit solution and the influence of BRB eccentricity on the seismic response.

This is an open access article under the terms of the Creative Commons Attribution License, which permits use, distribution and reproduction in any medium, provided the original work is properly cited.

© 2024 The Author(s). Earthquake Engineering & Structural Dynamics published by John Wiley & Sons Ltd.

¹Department of Civil, Environmental & Geomatic Engineering, University College London, London, UK | ²Department of Risk and Disaster Reduction, University College London, London, UK | ³Department of Structures for Engineering & Architecture, University of Naples Federico II, Naples, Italy | ⁴Department of Civil & Environmental Engineering, University of Liverpool, Liverpool, UK | ⁵Department of Civil and Mineral Engineering, University of Toronto, Toronto, Canada | ⁶Department of Civil Engineering, University of Patras, Patra, Greece | ⁷Department of Civil and Environmental Engineering, Myongji University, Seodaemun-gu, South Korea

1 | Introduction

Steel moment-resisting frames (MRFs) are commonly used as earthquake-resisting systems in building structures due to their architectural and constructional benefits, such as open facades and rapid construction. However, existing steel MRFs designed before modern seismic design codes have shown several performance shortcomings following large earthquakes, for example, [1–4]. While modern design codes, for example, [5, 6] have addressed most of these issues, many existing steel MRFs were designed under older regulations, lack adequate seismic detailing, and often require upgrades to enhance their performance. To this end, it is essential to develop reliable, effective, and easy-to-implement retrofit strategies to improve their seismic performance [7].

A viable and efficient retrofitting solution involves integrating buckling-restrained braces (BRBs) into existing frames. Compared to conventional braces, BRBs offer additional strength, stiffness, ductility, and, in turn, energy dissipation capacity. This is achieved using an unbonded restraining sleeve, which prevents the steel core from buckling, allowing nearly symmetrical hysteretic loops and large energy dissipating capacity [8–11]. Many research studies investigated the behavior of BRBs and their effectiveness in improving the seismic performance of newly designed and retrofitted structures, including large-scale experimental tests on reinforced concrete, for example, [12–16] and steel frames, for example, [17–22], extensive numerical studies, for example, [23–31] and the definition of optimal design methods, for example, [32–36].

BRBs are typically installed by aligning the diagonals within the plane of the frames. Thus, their installation requires the removal of non-structural components, such as infill walls, as part of the retrofit intervention. This process often results in prolonged business interruptions and additional retrofitting costs, representing one of the main limitations to the widespread application of this retrofit strategy. Various innovative solutions, such as exoskeletons, for example, [37-39], have been explored to overcome these challenges. In such solutions, the existing structure is retrofitted with braces placed externally to the frame [40, 41] or by connecting the structure to a parallel system, providing additional stiffness, strength, and ductility. This results in a reduction in the imposed seismic demand in the components of the existing frame, thereby protecting them from damage. Such solutions offer the advantage of minimal disruption to daily building use, making them highly favorable for practical implementation. However, aspects like integrating exoskeletons within steel frames and incorporating dissipative devices like BRBs have received limited attention and require further investigation.

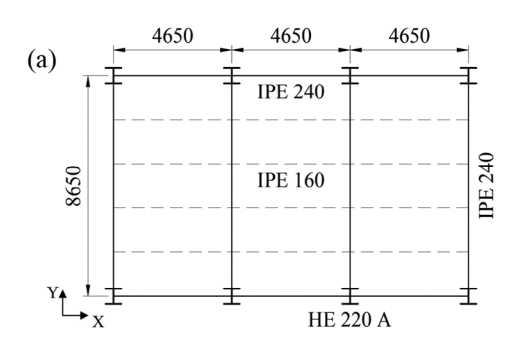
In such retrofit solutions, the design of the connections of the braces to the existing frame represents one of the most critical aspects. As highlighted by the AISC Design Guide 15 [42], seismic retrofit of existing steel buildings via bracings requires proper detailing of the connections that should be adequately stronger than the expected resistance of the connected braces. However, guidance is given for in-plane connections of internal braces, while no specific recommendations are provided for eccentric connections of externally located bracings. Design recommendations for conventional in-plane connections of both conventional

braces and BRBs can be found in the AISC standards [6] and in the second generation of Eurocode 8 [43], where a specific Annex provides rules and guidance for in-plane gusset connections of bracings internally placed into the main plane of the frame. However, neither North American nor European codes give recommendations for eccentric connections of externally placed bracings, even though such types of connections have specific features that may highly affect the rigidity, resistance, and ductility of the connected braces, that is, the deformability of the connections can limit the effectiveness of the bracing systems in developing their full ductility. The eccentricity is also responsible for secondary effects (e.g., torsion on columns and beams, bending in the minor axis of beams, and bending of braces) that may compromise the overall performance of retrofitted structures. Minimal research has been carried out in this direction, and there is a significant need for extended studies to define reliable design recommendations.

The present paper illustrates the second part of the experimental campaign carried out as part of the HITFRAMES ("HybrId Testing of an Existing Steel Frame with Infills under Multiple Earthquakes") project funded by the EU-H2020 SERA Consortium in Europe. HITFRAMES focused on the assessment and retrofitting of existing (i.e., non-seismically designed) steel MRFs and included large-scale Pseudo-Dynamic Hybrid testing (referred to as PsD in the rest of the paper) performed at the Structures Lab (STRULAB) of the University of Patras, Greece.

The case study building selected for the tests is a two-story steel MRF designed primarily for gravity loads with insufficient seismic detailing. The design of the case study building aimed to replicate the characteristics of an existing steel frame in Amatrice (Italy), which is considered to be representative of pre-code design scenarios and was extensively damaged after the 2016 Central Italy Earthquake [2]. The first part of the experimental campaign aimed to evaluate the performance of the existing frame, including the influence of masonry infills, and the results are summarized in Di Sarno et al. [44]. The second part of the experimental campaign discussed and elaborated in this paper focused on the seismic response of the structure retrofitted with BRBs.

The PsD tests were performed on the bare and retrofitted frame. The test specimen was a single frame of a two-story steel MRF, while the rest of the structure (i.e., the numerical substructure) was modeled in OpenSees [45]. In the retrofitted frame, the BRBs were installed considering a tailored connection, placing the BRBs eccentrically to the plane frame. Significant attention was placed on the connection details for BRBs and their influence on the response of the tested frame. PsD tests were performed for increasing intensities of the selected ground motion record. The experimental tests highlighted large torsional and distortional deformation in the parts of columns where the BRB connections were located, which was anticipated to be attributed to the eccentricity of the BRBs. The experimental results were essential to validate an advanced finite element (FE) model in ABAQUS [46] considering system- and local-level response parameters, including the above-mentioned torsional and distortional effects. Then, the paper investigates the effectiveness and optimization of the retrofitting strategy through parametric numerical FE analyses. The influence of BRB eccentricity on the seismic response is investigated, and the key parameters affecting the effectiveness of the solution are identified.



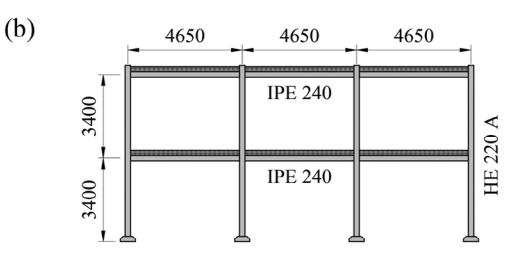


FIGURE 1 Prototype structure: (a) plan and (b) elevation views (units in mm).

The paper is organized as follows: Section 2 presents the case study structure and the relevant details; Section 3 summarizes the details of the performed PsD tests; Section 4 numerically investigates the influence of the BRBs eccentricity through a parametric FE analysis; Section 5 describes and discusses the response of structure with external BRBs; while Section 6 summarizes the main findings and conclusions.

2 | Case Study Steel Moment-Resisting Frame

2.1 | The Prototype Structure

Figure 1 shows the plan and elevation views of the prototype structure, which consists of a two-story, one-bay by three-bay non-seismically designed steel MRF. The building has a constant inter-story height of 3.4 m and bay widths of 4.65 and 8.65 m, respectively, along the x- and y-directions. The total dimensions of the building are 13.95 m by 8.65 m in plan and 6.8 m in height. The building was designed for gravity loads only following the European design code for steel buildings, Eurocode 3 (EC3) [47], assuming a non-structural permanent load equal to 2.58 kN/m² and an imposed load equal to 3 kN/m². Furthermore, as per the EC3, wind loads are considered negligible for low-rise structures, leading to a complete lack of lateral load-resisting systems in the frame design. The steel profiles were HE 220 A, IPE 240, and IPE 160, respectively, for columns, primary and secondary beams, with the weak axis of columns in the x-direction. A steel grade S355 (f_y = 355 MPa) was adopted for beams and columns. All primary beams were connected to columns through full penetration welds, and columns were fixed at the base. A 200-mm-deep concrete slab was also considered for each story. The mass of the prototype building was equal to 117.0 and 95.0 tons, respectively, for the first and second stories. The interested reader can refer to Di Sarno et al. [44] for additional details on the prototype structure.

2.2 | The Scaled Structure—Scaling and Similitude of the Prototype Building

The prototype structure was scaled down by a factor $\lambda = 0.75$ for the experimental tests according to the lab capabilities and following the same strategy used in Di Sarno et al. [44]. The prototype structure after scaling is then referred to as the "scaled structure" in the remaining part of the paper. The model scaling was implemented assuming acceleration and material scaling

TABLE 1 | Similitude scaling factors with $\lambda = 0.75$.

Parameter	Scaling factor
Density	$\lambda^{-1} = 1.33$
Stress, strain, angular deform., acceleration	$\lambda^0 = 1.00$
Period, time, velocity	$\lambda^{-0.5} = 0.87$
Length, linear deform., stiffness	$\lambda^1 = 0.75$
Force, weight, mass, area	$\lambda^2 = 0.56$
Volume, section moduli, moment	$\lambda^3 = 0.42$
Moment of inertia	$\lambda^4 = 0.32$

identity, as summarized in Table 1. Such a scaling factor (SF) is typically considered adequate for investigating the frame's seismic response at the global and local levels. As a result of the model scaling, the steel frame's story height and bay width were reduced to 2.5 and 3.5 m, respectively, and the columns' and beams' profiles became HE180A and IPE200.

2.3 | BRBs Design and Numerical Modeling

According to Eurocode 8-Part 3 (EC8-3) [5], the BRBs design should allow the retrofitted steel MRF to meet the requirements for a new structure, as per Eurocode 8-Part 1 (EC8-1) [43]. BRBs were installed in the central bay of the steel frames only; hence, a total of four BRBs (i.e., one per story of two parallel frames) were used for the retrofitting of the scaled structure. The BRBs were initially designed according to the procedure described in Gutiérrez-Urzúa and Freddi [30]. The design included modeling the frame in OpenSees [45], assessing the seismic performance of the existing structure, and designing the BRBs' properties to meet the design spectrum. However, the final choice for the BRBs used in the experimental campaign was dictated by the availability of the BRBs from the manufacturer. The selected BRB devices are the smallest ones available and represent a slightly overdesigned but still realistic solution to the seismic retrofit of the steel frame.

In this study, the BRBs were made by a series arrangement of an elastic brace and a BRB device [30]. The properties of the BRB devices adopted in the present study are provided in Table 2, where K_e is the elastic stiffness, F_y is the force at first yielding, d_u is the maximum allowable axial displacement, $F_{1,\ T}$ and $F_{1,\ C}$ are the yielding forces at stable hysteretic loops in tension and compression and $F_{u,\ T}$ and $F_{u,\ C}$ are the maximum forces in

TABLE 2 | Property of the selected BRB device for retrofitting the scaled structure.

				Ten	sion	Comp	ression
<i>L</i> (m)	K_e (kN/m)	F_y (kN)	d_u (mm)	$\overline{F_{1, T} (kN)}$	$F_{u,T}$ (kN)	$\overline{F_{1, C}(kN)}$	$F_{u,C}$ (kN)
1.535	88	125	20	167	175	191	225

tension and compression, respectively. The elastic braces had circular tube cross-sections with an external radius equal to 75 mm and a thickness of 10 mm.

2.4 | BRBs Connection Design

Figure 2 shows the geometry of the connection between the BRBs and the columns used for the specimen. The maximum effect due to the ultimately expected resistance of the BRBs (alternatively in tension and compression) was adopted to estimate the design demand on the bolted end-plate connections in terms of shear force, bending, and torsional moments. The eccentricity of the BRBs and their tilted position generate moments in both major and minor axes of the end-plate, as well as shear force and torsion. The resistance of end-plates was estimated in accordance with Eurocode 3–Part 1.8 (EC3-1-8) [48]. In particular, the biaxial moment resistance was evaluated, assessing the interaction domain in both major and minor axes of the

end-plate connection. The center of compression in the minor axis was assumed in the central vertical axis (where the vertical ribs are aligned), while one vertical line of bolts was considered active in tension. The moment resistance in the major axis was estimated assuming tension-active bolts solely those in the half part of the flange. In contrast, the center of compression was assumed in the centroid of the rib in the opposite half part of the connection. The shear forces due to torsional moment were estimated in all bolts assuming rigid in-plane flange, while the shear forces due to the applied action of the brace were calculated solely for the bolts in the compression zone.

3 | Pseudo-Dynamic Hybrid Simulation

The details of the experimental tests are illustrated hereafter. The specimen experimentally tested in the lab was the 1st bay plane frame of the *scaled structure*, as shown in Figure 3, and referred to as the *test specimen* in the following discussion.

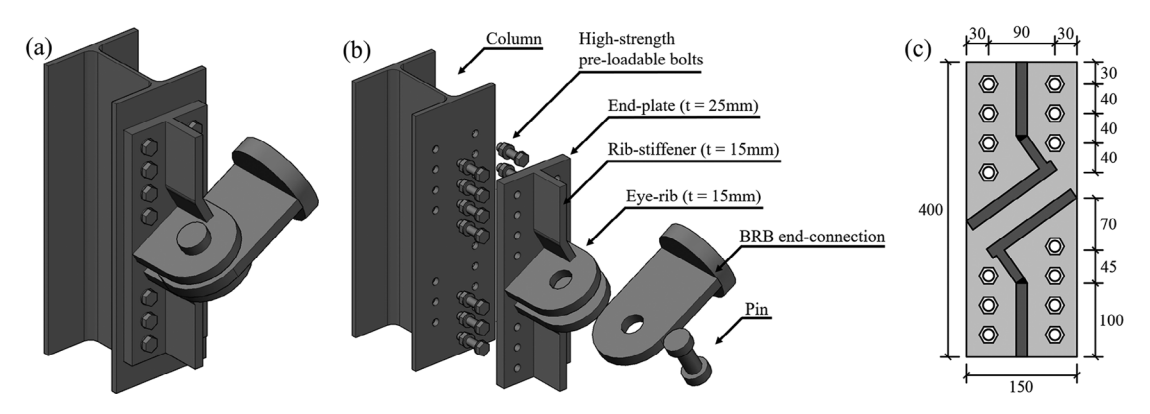


FIGURE 2 | BRB-to-column connection details: (a) geometrical configuration, (b) disassembled configuration, and (c) geometric dimension (units in mm). BRB, buckling-restrained brace.

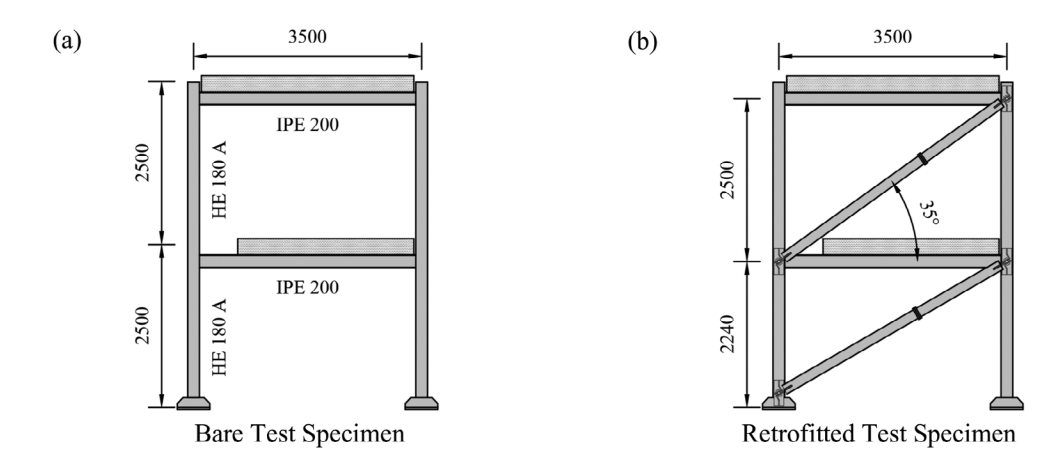


FIGURE 3 | Schematic view of the (a) bare and (b) retrofitted test specimens (units in mm).

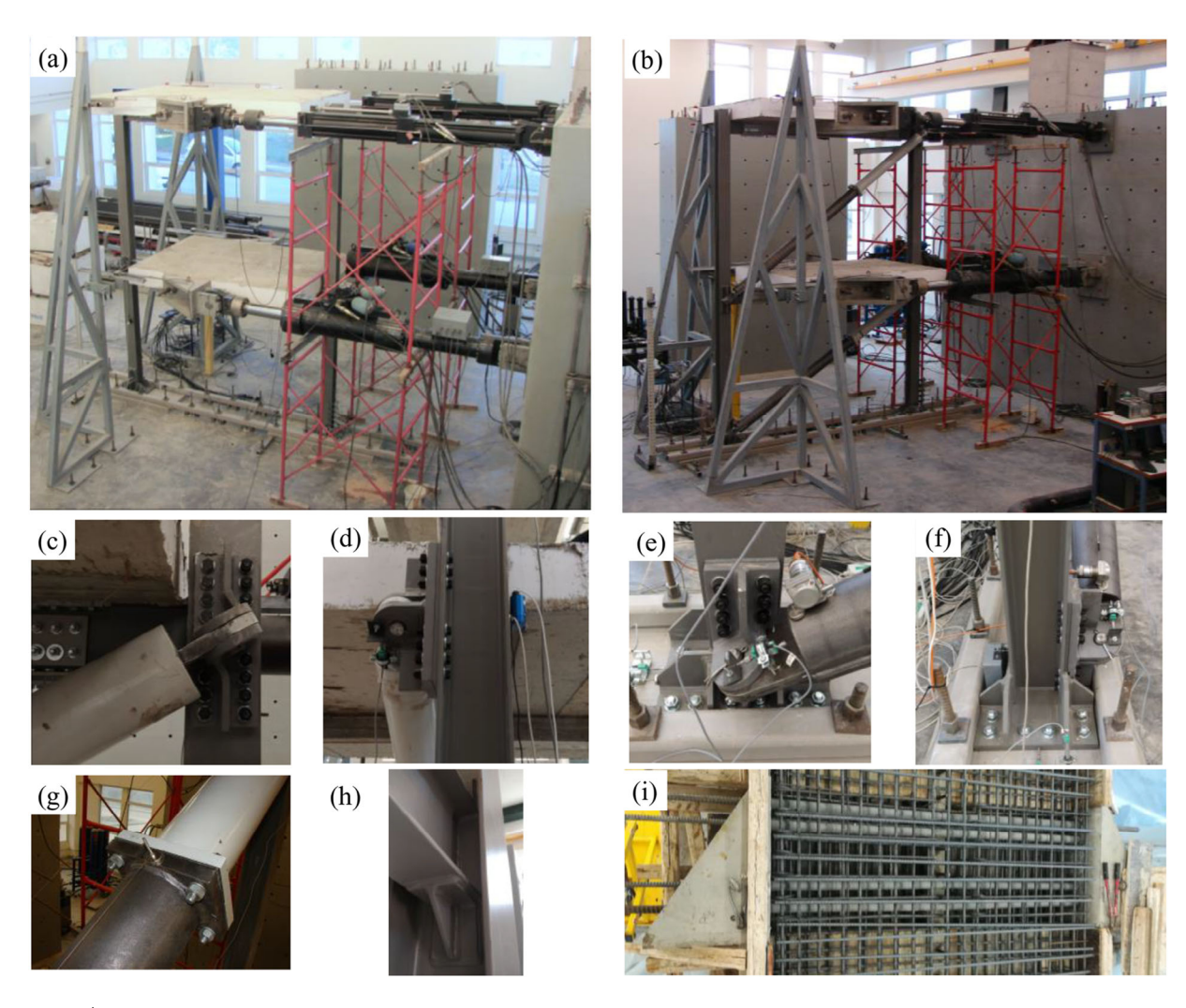


FIGURE 4 | (a) Test setup of the bare test specimen, (b) test setup of the retrofitted test specimen, (c through g) BRB's connection details, (h) beam-to-column connection, and (i) slab details. BRB, buckling-restrained brace.

Two configurations were considered, namely the *bare* and the *retrofitted test specimens*.

3.1 | Test Setup and Instrumentation

Figure 4 shows the bare (a) and retrofitted (b) test specimen setup, including details on the installation of the external BRBs (c to g). The test specimen was built based on the common European construction practice. The steel frame was welded and prepared in the workshop and fully assembled in the laboratory. As shown in Figure 4a,b, four actuators were employed to conduct the PsD tests, with two connected to the slab at each story. The connection between actuators and slabs was designed to ensure a smooth transfer of stress from the actuators to the test specimen, as shown in Figure 4i. Two parallel tubular beams were placed on top of the column base plates and anchored to the strong floor of the lab, as shown in Figure 4f, in order to increase the rigidity of the base restraints of the test setup. The concrete slab was built following the construction of the steel frame. It is worth mentioning that stiffeners were also adopted to increase the rigidity of the beam-column connections, as shown in Figure 4h. Figure 4g shows the connection between the bracing system and the BRB device. Moreover, Figure 4c-f shows the eccentric pin connections of the BRBs to the external flange of the columns.

Additionally, coupon tests were performed on steel pieces extracted from beams and columns of the test specimen and conducted according to the BS EN ISO 6892-1 [49] standard. The experimental mean yield strength and ultimate strength of S355 steel were 424 and 575 MPa, respectively.

The instrumentation for the PsD tests was designed to monitor the response of the test specimen. Figure 5 schematically shows the key sensors used in the experimental tests, the results of which are used in the present paper to validate the FE models. In the free vibration test, four accelerometers and four displacement-measuring optical devices (OPT1 to OPT4 in Figure 5) were used to monitor the story displacements and accelerations. Besides, two potentiometers (DTB1 and DTB2 in Figure 5) were placed to monitor any story transversal displacement. Then, during the PsD tests, the accelerometers were removed from the test setup. At the same time, a range of additional sensors were installed to monitor the joint rotations, the column deformations along the height of the expected plastic hinge zone, and the diagonal

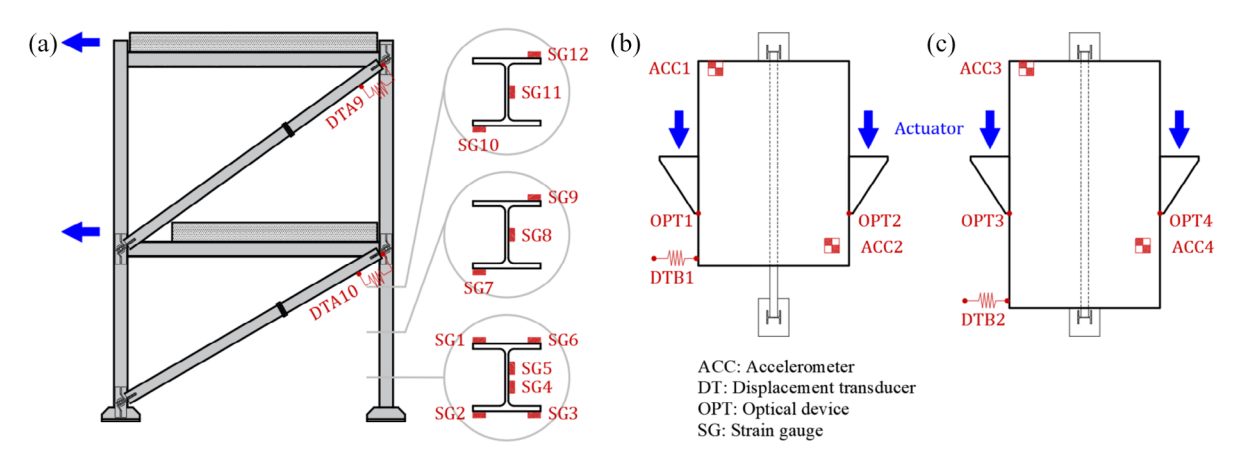


FIGURE 5 | Location of the key sensors for monitoring the response of the steel frame: (a) BRB test specimen, (b) first floor, and (c) second floor. BRB, buckling-restrained brace.

elongation of both stories, as illustrated in Figure 5. Furthermore, twelve strain gauges were employed to measure strains induced in the selected column, as shown in Figure 5. The axial force and deformation of BRB devices were also monitored during the tests (DTA9 and DTA10 in Figure 5). The complete description of the instrumentation used in the tests and the full data set is provided in Bousias et al. [50].

3.2 | Ground Motion Record Selection

The East-West component of the August 24, 2016, Central Italy earthquake recorded at the Station in Norcia, Italy (NRC) was used in the PsD tests. Such strong motion was considered representative of areas with moderate- to high seismicity in Southern Europe. It was characterized by large spectral accelerations in the range of natural periods corresponding to bare and retrofitted

TABLE 3 | Information of the selected ground motion record for the Pseudo-Dynamic Hybrid tests.

Date	M_w (-)	R_{epi} (km)	PGA (g)
August 24, 2016	6.0	15.3	0.35

Note: ID EMSC-20160824_0000006, Station in Norcia, Italy (NRC)-East-West component of the ground motion. Source: https://esm.mi.ingv.it/.

frames. Table 3 reports the main information of the selected record, including the moment magnitude (M_w) , epicentral distance (R_{epi}) , and peak ground acceleration (PGA). The ground motion record was obtained from the Engineering Strong-Motion database (ESM) [51]. The earthquake time history was scaled in time by a factor of 0.87 according to the similitude scaling in Table 1. Figure 6a shows the accelerogram of the ground motion scaled in time, while Figure 6b,c shows its response spectra.

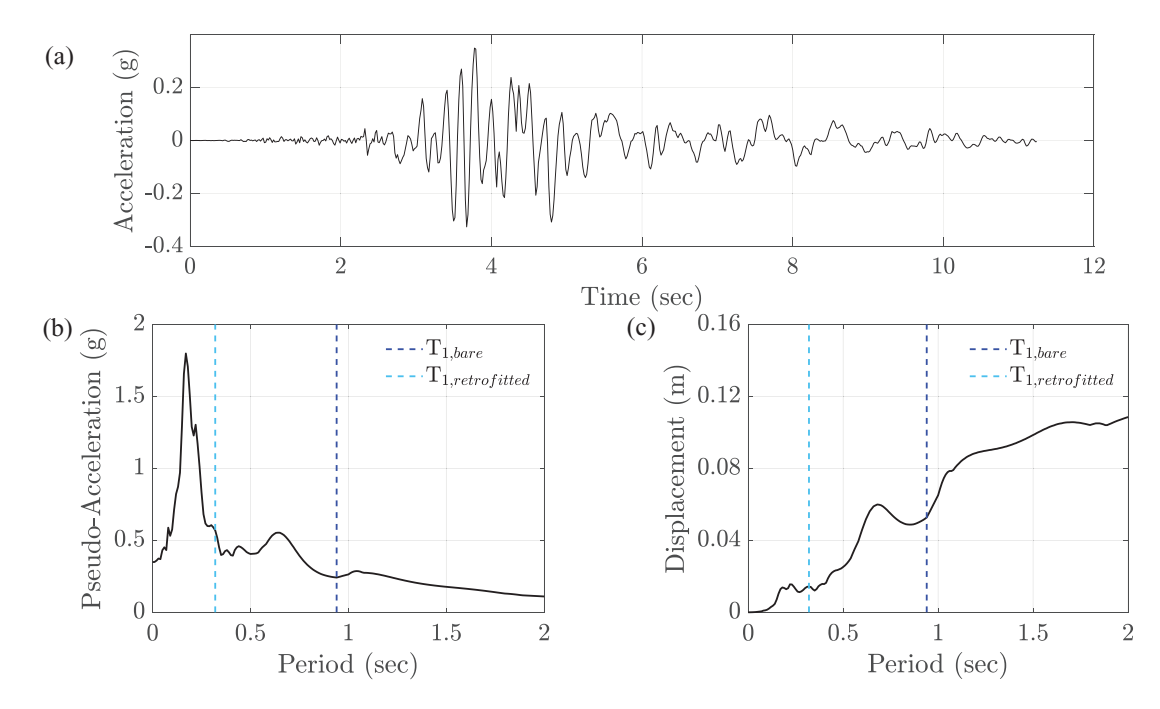


FIGURE 6 | Selected ground motion record: (a) accelerogram, (b) acceleration response spectrum and natural periods of the scaled structure, and (c) displacement response spectrum.

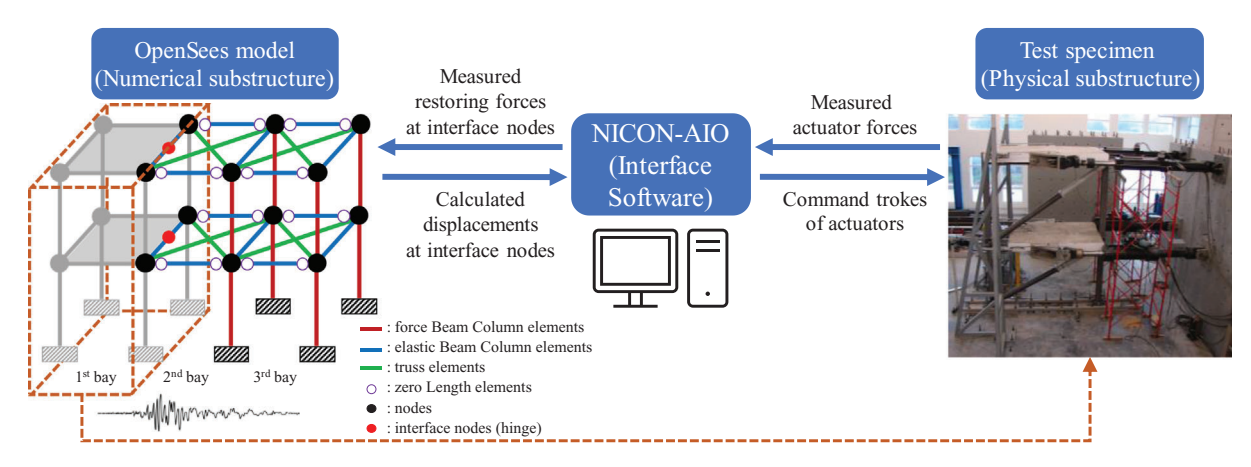


FIGURE 7 | Integration of the numerical and physical substructures in the hybrid simulation using NICON-AIO.

3.3 | Implementation of the Hybrid Simulation

In hybrid simulation, the target structure is divided into two parts: a numerical substructure and a physical substructure. A part of the target structure whose behavior is of interest or challenging to simulate numerically is tested in the laboratory (i.e., the test specimen). In contrast, the rest of the target structure is modeled, typically using the FE method, and numerically considered during the test (i.e., the numerical substructure). This approach allows for an efficient and cost-effective investigation of the behavior of the system without the need to physically test the whole structure.

In the hybrid simulation of this study, the 2nd and 3rd bays, which are not retrofitted by BRBs, were considered as the numerical substructure. OpenSees [45] was used for modeling the numerical substructure. In the model, the columns were modeled with forceBeamColumn element, while the beams were modelled with elasticBeamColumn elements. For the beams in the lateral direction, zeroLength elements were added at both ends of the beam elements to represent plastic hinges. Steel01 material was used for the columns, and Hysteretic material was used for the beam hinges. The slabs were modelled with rigid truss elements to represent a rigid diaphragm. Figure 7 illustrates how the numerical substructure was modelled and integrated with the physical substructures in the hybrid simulation. At each time step of the test, the response of the target structure subject to the input ground motion was calculated through numerical integration, including the displacements at the interface between the numerical and physical substructures. The alpha-operator splitting method [52] was used for the numerical integration. The interface between the numerical and physical substructures was assumed to be pin-connected, thereby transmitting no bending moment through the interface. Thus, the interface was modeled with hinge nodes in the OpenSees model (highlighted in red dots in Figure 7). The calculated displacements in the lateral direction at the interface were imposed on the test specimen by controlling the four actuators mounted on it. Subsequently, the restoring force of the test specimen was measured from the actuators, which was fed back to the OpenSees model to calculate

TABLE 4 Test matrix for the bare and retrofitted steel frame.

	Test	Description
		BRB component test
	1	Snap-back free-vibration test of the bare frame
en	2	PsD test of the bare frame (SF = 0.35)
cim	3	PsD test of the bare frame (SF = 0.75)
Test specimen	4	PsD test of the bare frame (SF = 1.00)
Test	5	PsD test of the retrofitted frame (SF = 1.00)
	6	PsD test of the retrofitted frame (SF = 1.50)

displacements for the next time step. This process was repeated throughout the hybrid simulation.

To efficiently perform the above-mentioned process during the test, an interface software called NICON-AIO was used. The NICON-AIO was developed based on the generalized hybrid simulation framework UT-SIM (www.ut-sim.ca) [53], which incorporates a variety of functionalities required to run the hybrid simulation, such as data exchange and communication between the numerical and physical substructures, coordinate transformations between the calculated and measured displacements and forces, scaling of the measured displacements and forces for small-scale test specimens, ramp generation for actuator control, error compensation, and limit checks. Further details on the NICON-AIO can be found elsewhere [54, 55].

3.4 | Test Matrix

The test matrix is summarized in Table 4. This includes the component test of one BRB and several tests of the test specimen. The test specimen was first subjected to a snap-back free vibration test in its bare configuration. A set of PsD tests was then performed on both the bare and retrofitted configurations, considering incremental intensities of the ground motion record,

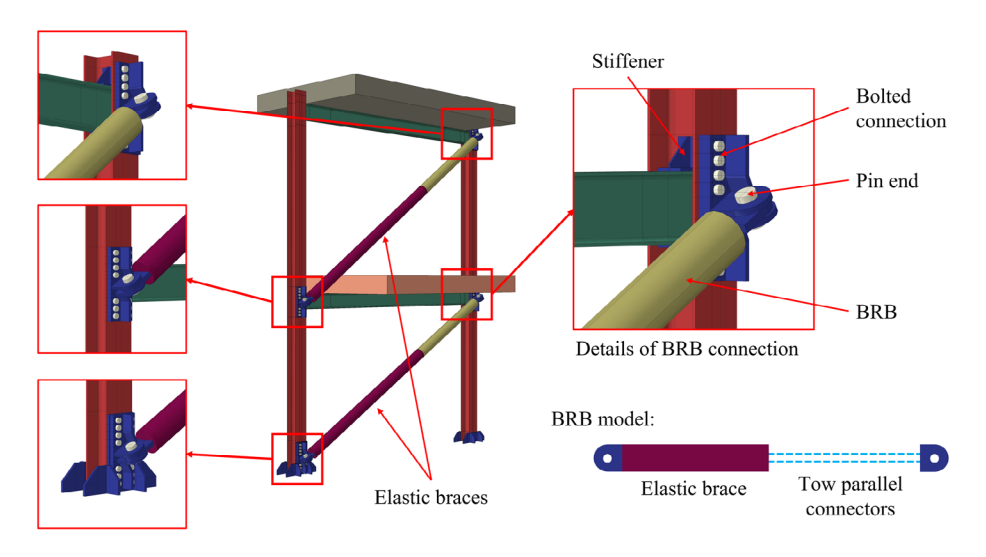


FIGURE 8 | Finite element (FE) modeling of the test specimen retrofitted with BRBs. BRBs, buckling-restrained braces.

with SFs ranging from 0.35 to 1.50. The SF = 1.5 was adopted to ensure the yielding of BRBs, such that the full behavior of BRBs could be observed during the test. The final test with SF = 1.5 was terminated due to large torsional effects in the columns.

3.5 | Test Results and Numerical Modeling

A refined FE model was built in ABAQUS [46] to investigate the seismic performance of the retrofitted frame. In addition to the OpenSees model used for the PsD tests, the ABAQUS model allows investigating the influence of the local details and expanding the results through parametric numerical simulations. Details of the ABAQUS model are presented in Figure 8. All steel components (i.e., beams, columns, plates, and stiffeners) were modeled using the C3D8R solid element, which is a generalpurpose linear brick element with reduced integration points. Young's modulus and Poisson's coefficient of the steel were assumed to be 210 GPa and 0.3, respectively, while its plastic behavior was defined by a yield stress of 424 MPa and a hardening ratio of 0.02 according to the results of the coupon tests. Besides, beams were connected to the web of columns through tie constraints to simulate the full penetration welds. Similarly, the stiffeners were also connected to beams and columns through tie constraints. The concrete slabs in the FE model were also modeled using C3D8R solid elements, which were simplified as homogeneous concrete blocks with Young's modulus equal to

35,000 MPa. The plastic behavior of the concrete slabs was not defined in the present study since no evident cracking was noticed during the PsD tests. The slab was connected to the top flange of beams through tie constraints. Lastly, fixed boundary conditions were imposed on the bottom of columns and adjacent stiffeners.

In the retrofitted test specimen, the BRB devices and elastic braces were modeled separately, as shown by the BRB model in Figure 8. The elastic braces were explicitly modeled as steel tubes, while the BRB devices were simulated by two parallel axial connectors. In Figure 8, the layout of the BRB devices is included for visualization purposes only, as connector elements do not have a physical shape. The elastic stiffness of the BRB devices, that is, the combined elastic stiffness of the two connectors, was equal to 88000 N/m. On the other hand, their plastic behavior involved the definition of two types of non-linear hardening, that is, isotropic and kinematic hardening. The isotropic hardening was solely defined by one of the connectors. Conversely, both connectors were individually assigned the parameters to define their kinematic hardening, such that the "true" kinematic hardening of the BRB device could be better captured. The parameters calibration was performed against the experimental cyclic tests of a BRB device, as discussed in the following section.

Figure 9 shows the mesh for the relevant elements of the FE model. A specific mesh density has been identified per element to obtain a consistent stress and strain distribution. In particular,

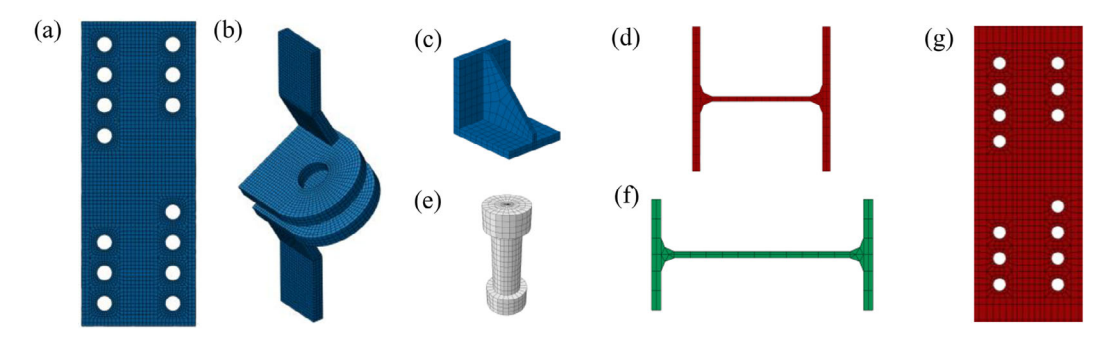


FIGURE 9 | Adopted mesh for: (a) end-plate, (b) eye-rib, (c) beam-to-column connection stiffener, (d) column, (e) bolt, (f) beam, and (g) column flange in the connection zone.

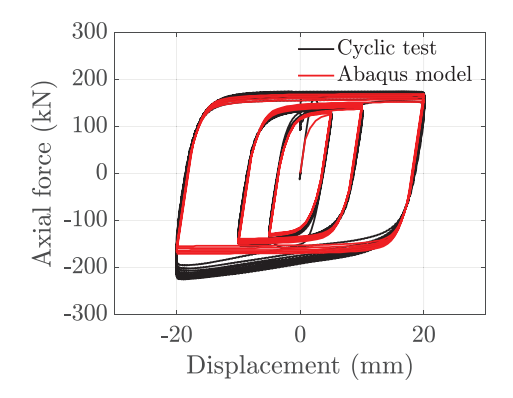


FIGURE 10 | Cyclic response of the BRB device: Experimental versus numerical results. BRB, buckling-restrained brace.

end-plates (Figure 9a), eye rib (Figure 9b), and bolts (Figure 9e) were discretized by means of a 5 mm mesh, while an approximate element dimension of 10 mm was used for beam-to-column connection stiffeners (Figure 9c). Beam and column profiles were meshed with elements of 10 mm in the connection zones and 25 mm in the remaining regions (Figure 9d,f,g).

3.5.1 | Cyclic Test of BRB Devices

The behavior of the adopted BRB devices was experimentally investigated through a cyclic test. The loading scheme involved five cycles at ± 5 and ± 10 mm, respectively, and ten cycles at ± 20 mm, which is the maximum allowable deformation of the adopted BRB device. The obtained cyclic response of the BRB device is presented in Figure 10. The adopted BRB device had a capacity of ~ 175 and ~ 225 kN in tension and compression, respectively, consistent with the properties provided by the manufacturer, as summarized in Table 2.

The properties of the two connectors used for the FE model of the BRB device are reported in Table 5. The hardening behavior of such connectors is controlled by Equations (1) and (2). Equation (1) describes the yield surface size for non-linear isotropic hardening, where F^0 represents the yield surface defined as a function of the equivalent plastic deformation \bar{u}^{pl} , $F|_0$ is the yield force at zero plastic deformation, Q_{inf} is the maximum increase in the size of the yield surface, and b is the rate at which the yield surface increases. On the other hand, Equation (2) describes the non-linear kinematic hardening, where α is the backforce, and u^{pl} is the plastic deformation. Moreover, C and γ are parameters calibrated from the test data, which respectively

TABLE 5 | Parameters defining the non-linear isotropic and kinematic hardening of the cyclic behavior of the simplified BRB model using connectors.

	$F _0$ (kN)	Q_{inf} (kN)	b	C (kN/m)	γ
Connector 1	75	75	0.003	55	1.25
Connector 2	_	_	_	3	0.25

represent the initial kinematic hardening modulus and the rate of the decrease of the kinematic modulus with increasing plastic deformation. In the present study, two pairs of C and γ parameters were used to describe the kinematic hardening of the BRBs; hence, two parallel connectors were included in the model

Figure 10 shows a satisfactory match between the cyclic experimental and numerical results of the BRB device. However, some limitations can be observed. The model was able to correctly simulate the capacity in tension (i.e., ~175 kN); however, the built-in material model in ABAQUS was unable to correctly reproduce the asymmetric behavior in compression, that is, the capacity in compression is the same as in tension, resulting in ~22% lower force than the actual capacity. The use of a compression-only spring could compensate for the extra capacity in compression, as done in the study by Tsai et al. [56]. However, this approach was not followed in the present study. The adopted strategy was considered the best compromise between the complexity of the model and the accuracy of the results. This difference in the experimental and numerical results at the component level only had a limited impact on the final numerical simulations, as demonstrated and discussed afterward.

$$F^{0} = F|_{0} + Q_{inf} \left(1 - e^{-b\bar{u}^{pl}} \right) \tag{1}$$

$$\alpha = \frac{C}{\gamma} \left(1 - e^{-\gamma u^{pl}} \right) \tag{2}$$

3.5.2 | Test Results and Validation of FE Models

The snap-back tests allowed the calibration of the stiffness of the FE model for the bare configuration corresponding to $T_{I,bare}=0.532$ s. The numerical simulations of the PsD tests were performed by applying the story displacement histories recorded during the PsD tests to the FE model, allowing a direct comparison of the results. Figures 11 and 12 show the experimental versus numerical results for the bare test specimen for Test 4 (SF = 1.00–see Table 4). The results of the bare test specimen were used for FE model calibration at global and local levels.

Figure 11a shows the story displacement histories, while Figure 11b,c shows the comparison of the story shear forces. The bare test specimen experienced a maximum inter-story drift ratio (IDR) of ~1.8% and ~2.5% at the first and second stories, respectively. Figure 12 shows the experimental versus numerical results for the strains in one of the columns (see Figure 5 for the position of strain gauges). Minor yielding occurred at the base of the monitored column, with strain recordings slightly exceeding the yield strain of ~0.002 (i.e., SG2 and SG6). Such comparisons show an excellent agreement between the experimental versus numerical results at both global and local levels. The maximum error between the experimental and numerical results was approximately 15%.

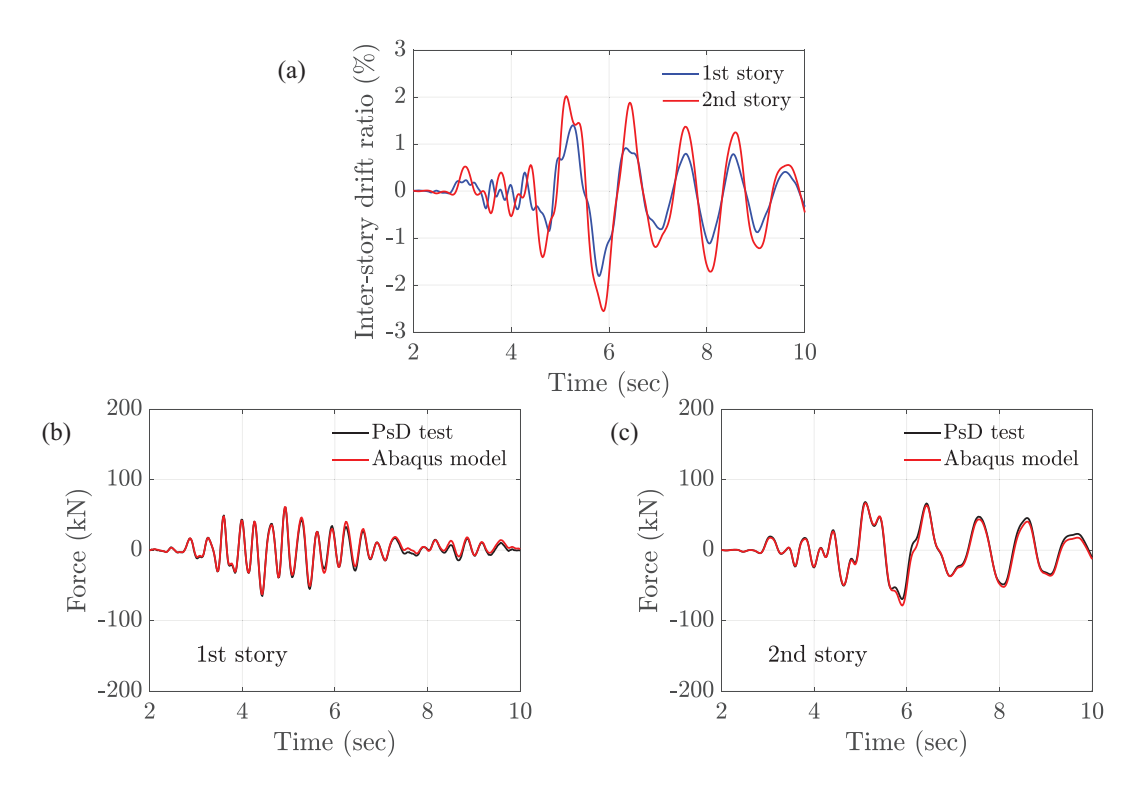


FIGURE 11 Experimental versus numerical results for the bare test specimen for Test 4 (SF = 1.00–see Table 4). (a) Displacement time histories at the 1st and 2nd story, (b) story shear at the 1st story, and (c) story shear at the 2nd story.

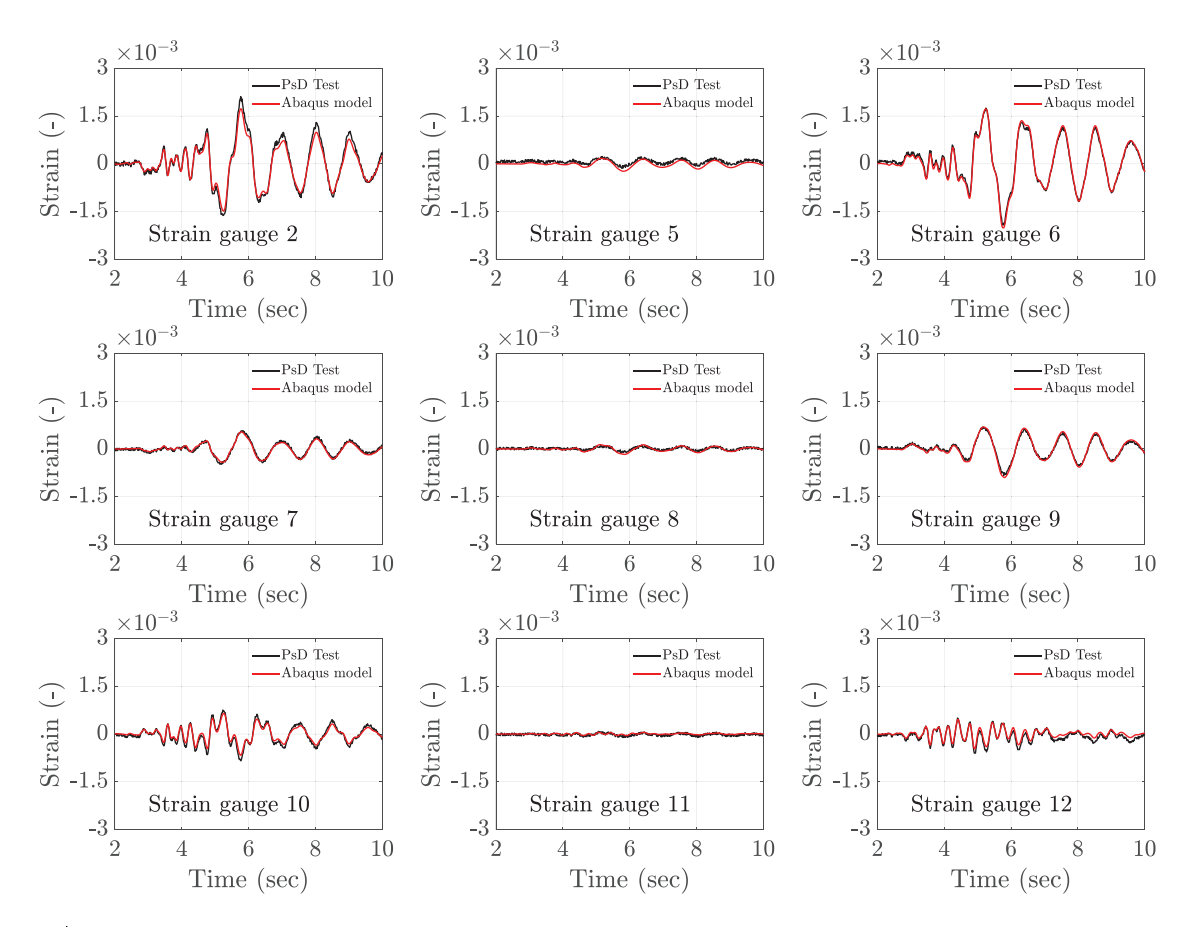


FIGURE 12 Experimental versus numerical results for the bare test specimen for Test 4 (SF = 1.00–see Table 4). Strain gauges readings at different locations in a first story column (see Figure 5 for strain gauge location).

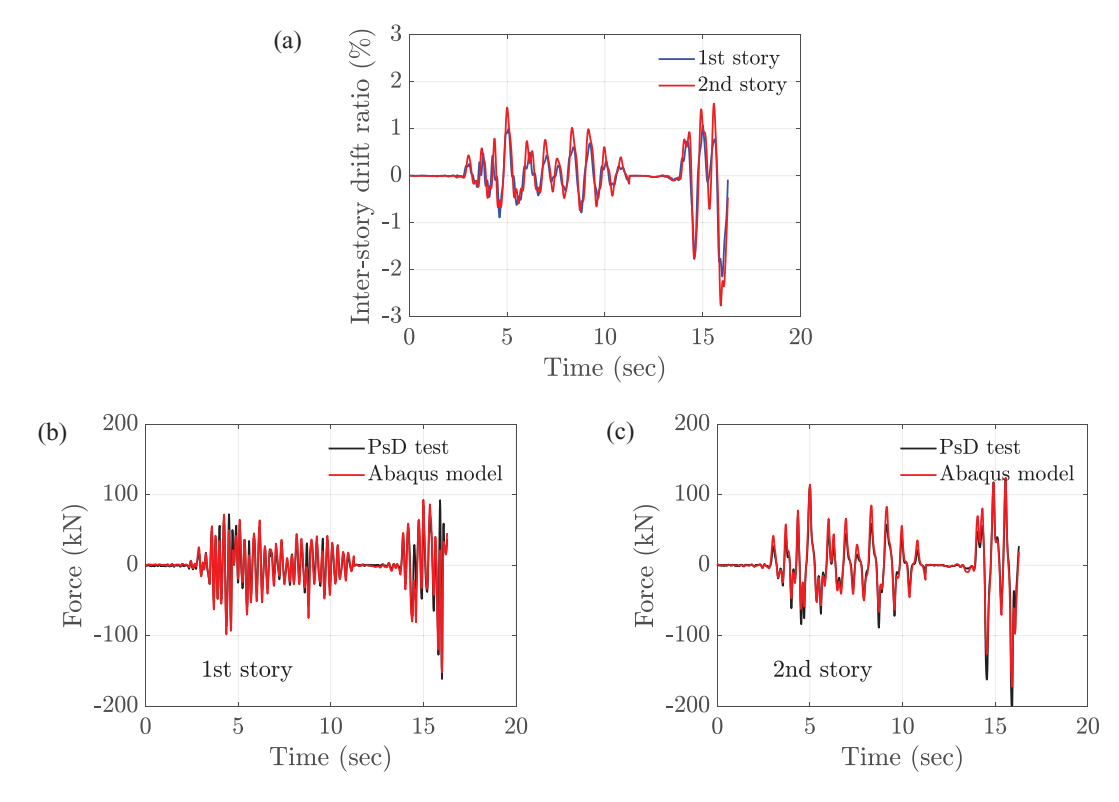


FIGURE 13 | Experimental versus numerical results for the retrofitted test specimen for Tests 5 and 6 (SF = 1.00 and 1.50-see Table 4). (a) Displacement time histories at the 1st and 2nd story, (b) story shear at the 1st story, and (c) story shear at the 2nd story.

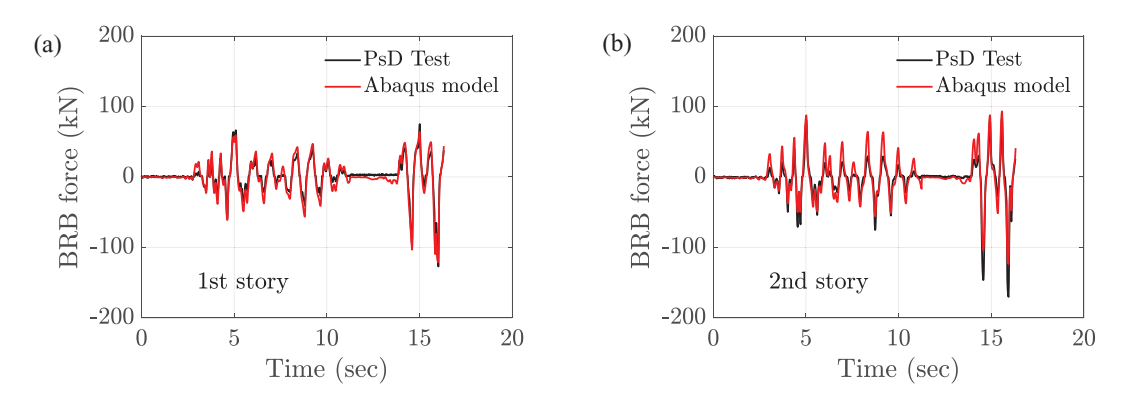


FIGURE 14 Experimental versus numerical results for the retrofitted test specimen for Tests 5 and 6 (SF = 1.00 and 1.50–see Table 4). Axial forces in BRBs at (a) 1st and (b) 2nd story. BRBs, buckling-restrained braces.

Figures 13, 14, and 15 show the experimental versus numerical results for the retrofitted test specimen for Tests 5 and 6 (SF = 1.00 and 1.50–see Table 4). Test 5 was completed by applying the full acceleration time-history. Conversely, Test 6 was interrupted after approximately 4 s of the time-history due to excessive torsional deformations in the columns and out-of-plane displacements of the frame.

Figure 13a shows the story displacement histories highlighting that, during Test 5 (SF = 1.0), the introduction of the BRBs reduced the maximum IDRs to \sim 0.9 and \sim 1.5%, respectively, at the first and second story. These values are \sim 50% and \sim 40% smaller than those recorded during the test of the bare specimen. Besides, during Test 6 (SF = 1.5), the maximum IDRs reached

values of \sim 2.2% and \sim 2.8%, respectively, at the first and second stories, after which the test was stopped. Figure 13b,c shows the comparison of the story shear forces. These results showed that the FE model slightly underestimates the shear force in the negative direction (i.e., with the BRBs in compression).

Figure 14 shows the experimental versus numerical results for the forces in the BRBs. The FE model tends to slightly overestimate the BRBs forces in tension and underestimate them in compression, with an error of up to 35%. This was due to several reasons, including the limitations of the BRBs modeling previously discussed and the tolerance in the pin connection of BRBs, which played a role in the experimental response. This tolerance was not included in the ABAQUS model, leading to overestimating

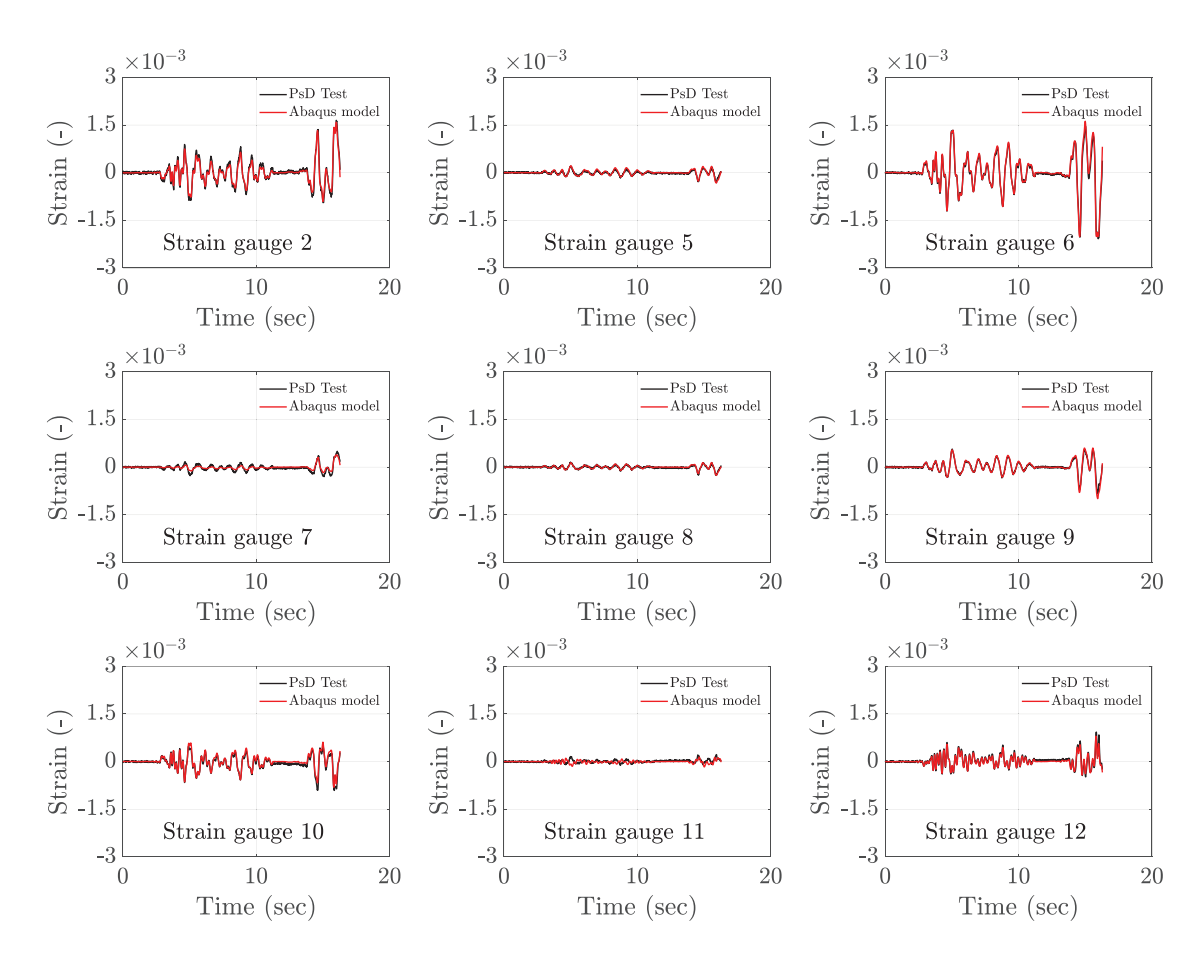


FIGURE 15 Experimental versus numerical results for the retrofitted test specimen for Tests 5 and 6 (SF = 1.00 and 1.50–see Table 4). Strain gauges readings at different locations in a first story column (see Figure 5 for strain gauge location).

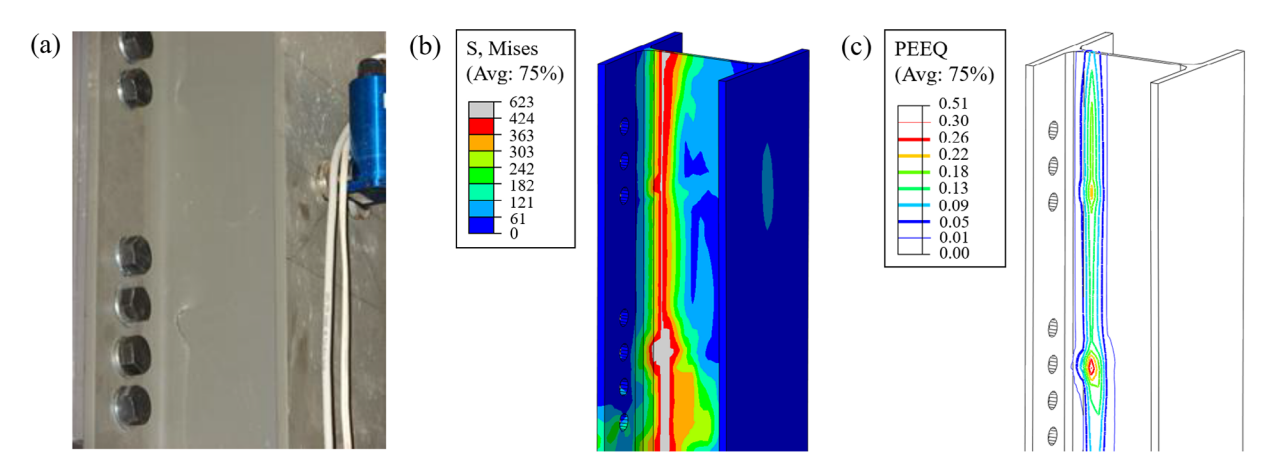


FIGURE 16 | Experimental versus numerical results for the retrofitted test specimen after Test 6 (SF = 1.50–see Table 4). Damage observed in the test specimen versus (b) stress distribution and (c) PEEQ and in the numerical model.

the forces in BRBs, especially for small displacements. Despite the differences in terms of story shear and forces in BRBs, Figure 15 shows an excellent agreement in terms of experimental versus numerical strains in the monitored column, characterized by a maximum error of 15% (see Figure 5 for the position of strain gauges). Lastly, Figure 16 shows the damage observed in one of the columns of the test specimen at the end of Test 6. It can be observed that the column web was fractured at the connection zone due to excessive torsional and distortional deformations.

Such damage was anticipated from the FE model, which shows high-stress concentration (Figure 16b) and equivalent plastic strain (PEEQ, Figure 16c) where the fracture occurred. Overall, the comparisons show a satisfactory agreement between the experimental versus numerical results at both global and local levels.

Although some simplifications were introduced in the model, in the Authors' opinion, the adopted strategy is the optimal

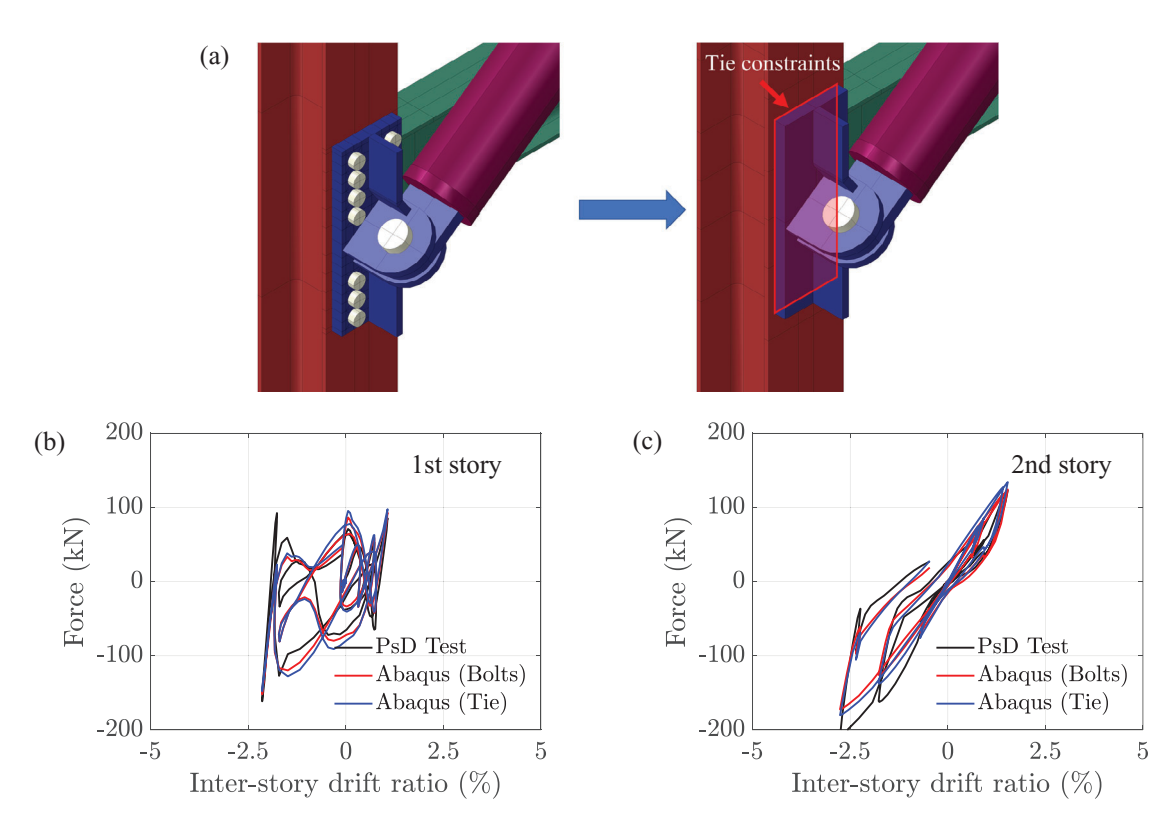


FIGURE 17 | Validation of the simplification of bolted connections using tie constraints: (a) complex versus simplified modeling strategy, (b) response of the first story, and (c) for the second story during Test 6 (SF = 1.50–see Table 4).

compromise in terms of computational efficiency and accuracy of the results.

3.6 | Simplification of Bolted Connections

To further reduce the computational effort in numerical simulations, a simplified model was introduced to simulate the connection between the flush end-plate of BRBs and the flanges of columns. In particular, the complex connection simulating contacts and pre-loads in the bolts was simplified by a tie constraint, as shown in Figure 17a. Figure 17b,c compares the story shear versus IDRs for the first and second stories during Test 6. The comparison highlights that the complex (i.e., bolts modeling) and simplified (i.e., tie constraint) modeling strategies show similar results. Hence, such simplification was adopted for the following analyses.

4 | Evaluation of the Influence of BRB Eccentricity

The outcomes of experimental tests in the previous section highlighted the expected torsional and distortional deformation in columns due to the BRBs eccentricity and allowed the validation of a detailed numerical model. Such a model is used in the present section to further investigate the influence of BRBs eccentricity through a parametric analysis. An equivalent numerical model of the steel frame with in-plane BRBs was created and used as a benchmark for comparison with different configurations incorporating external BRBs. A parametric analysis was conducted to

investigate the influence of the torsional and distortional stiffness of columns on the seismic response of frames with external BRBs.

The FE models used in this section focus on the same steel frame and retrofit configuration investigated in the PsD tests. The BRBs were assumed to possess the same mechanical properties described in Figure 10. Nonetheless, as the adopted FE model could not capture the asymmetric behavior of the BRB devices under cyclic loading, pushover analyses were performed separately in the tensile and compressive directions. To this end, the FE model of the BRB devices was updated using the same twoparallel-connector configuration but with modified properties assigned to each connector, as summarized in Table 6. The isotropic hardening was not defined in this case, as it was not required in pushover analysis. However, an elastic connector was adopted in the BRB model to simulate yield stress increase due to isotropic hardening, as shown in Figure 18. For the sake of brevity, the following section presents the results of pushover analysis only for the BRBs subjected to tensile forces. Similar considerations can be made for BRBs subjected to compressive forces.

TABLE 6 | Parameters defining the monotonic behavior of the connectors in the modified BRB models.

		K (kN/m)	F_y (kN)	C (kN/m)	γ
Tens	Connector 1	86	68	65	1.25
	Connector 2	2	_	_	_
Comp	Connector 1	83	66	65	1.25
	Connector 2	5	_	_	_

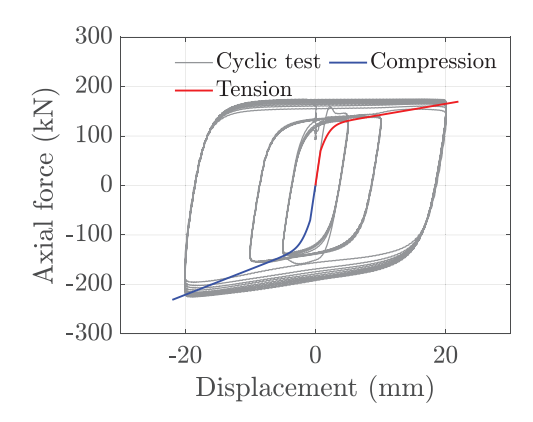


FIGURE 18 | Cyclic response of the BRBs: Comparison between the test results and numerical simulation. BRBs, buckling-restrained braces.

4.1 | Parameters Affecting the Effectiveness of External BRBs

The parametric analysis considers six FE models, as summarized in Table 7 and Figure 19. Such models consider different positions of BRBs (i.e., in-plane and external) and different constraints to avoid the torsional and distortional effects in the columns. Such constraints are included to simulate the contribution that could be achieved from tailored steel plates to increase the stiffness of the connection and/or the stiffening contribution of the concrete slab. Additional details about the practical implementation of possible constraints are provided in Section 5. It is worth mentioning that torsional and distortional constraints (TCDC) were applied to the middle section of columns within each connection zone (see Figure 19d).

Figure 19a shows the steel bare frame (Model 1–BARE), while Figure 19b shows the steel frame retrofitted with BRBs placed in-plain within the frame (Model 2–BRB_INP), representing the benchmark BRBs structure. Conversely, Figure 19c shows the global configuration of the steel frame retrofitted with BRBs placed externally, as done in the PsD test, and with no additional constraints (Model 3–BRB_EXT). The above three models are referred to as the reference models in the following discussion.

Three additional models were built based on the same global configuration of Model 3 -BRB_EXT but with the inclusion of TCDC applied to the columns, as illustrated in Figure 19d. Model

4-BRB_EXT_TCDC included TCDC. A rigid body constraint was used to prevent the distortional deformation of column flanges, which tied the displacements of each controlled cross-section of columns to the displacements of the reference point located at its geometric center. Boundary conditions were applied to the reference point to restrain the out-of-plane displacement and rotation of the controlled sections, thus preventing torsional deformations. Model 5-BRB_EXT_TC included only the torsional constraint (TC). The torsional deformation at the controlled sections was avoided by restraining the inner flanges' out-of-plane displacement, while the section distortion was permitted. Lastly, Model 6-BRB EXT DC included only the distortional constraint (DC). The distortional deformation of flanges was restricted by using the rigid body constraints as in Model 4. However, no additional boundary conditions were implemented at the reference point, thus allowing the torsional deformation of the section.

The results of the pushover analyses of the different configurations are presented in Figure 20 in terms of story shear versus IDRs. The end of each pushover curve represents the failure of BRBs due to maximum axial deformation (i.e., 20 mm in this study). These figures show how the BRBs retrofitting strategy results in a substantial increase in stiffness and strength. The comparison between BRB_INP and BRB_EXT (i.e., frames with in-plane and external BRBs) highlights how torsional and distortional deformations in the columns affect the stiffness of the frame and force transfer mechanism within the devices. For instance, the lateral stiffness of BRB_INP was over five times that of BRB_EXT. It can thus be highlighted how the BRB_EXT results in lower plastic deformations in the BRBs and, hence, lower energy dissipation compared with the BRB INP.

Figure 20 shows how the BRB_INP and BRB_EXT_TCDC yield similar results, indicating that the use of in-plane BRBs is approximately equivalent to the use of external BRBs with restricted torsional and distortional deformability of columns in the connection zones. This confirms the importance of these two key parameters in controlling the effectiveness of the retrofit strategy with external BRBs. Figure 20 also shows the comparison of the BRB_EXT_TC with the reference models, highlighting that the TCs alone do not improve the performance of the retrofitted frame. Similarly, the comparison of the BRB_EXT_DC with the reference models shows that the DCs led to a nearly 100% increase in the initial stiffness of the model BRB EXT.

TABLE 7 Adopted FE models to investigate the influence of BRB eccentricity.

Model	Label	BRB position	Torsional constraint (TC)	Distortional constraint (DC)
1	BARE	None	No	No
2	BRB_INP	In-plane	No	No
3	BRB_EXT	External	No	No
4	BRB_EXT_TCDC	External	Yes	Yes
5	BRB_EXT_TC	External	Yes	No
6	BRB_EXT_DC	External	No	Yes

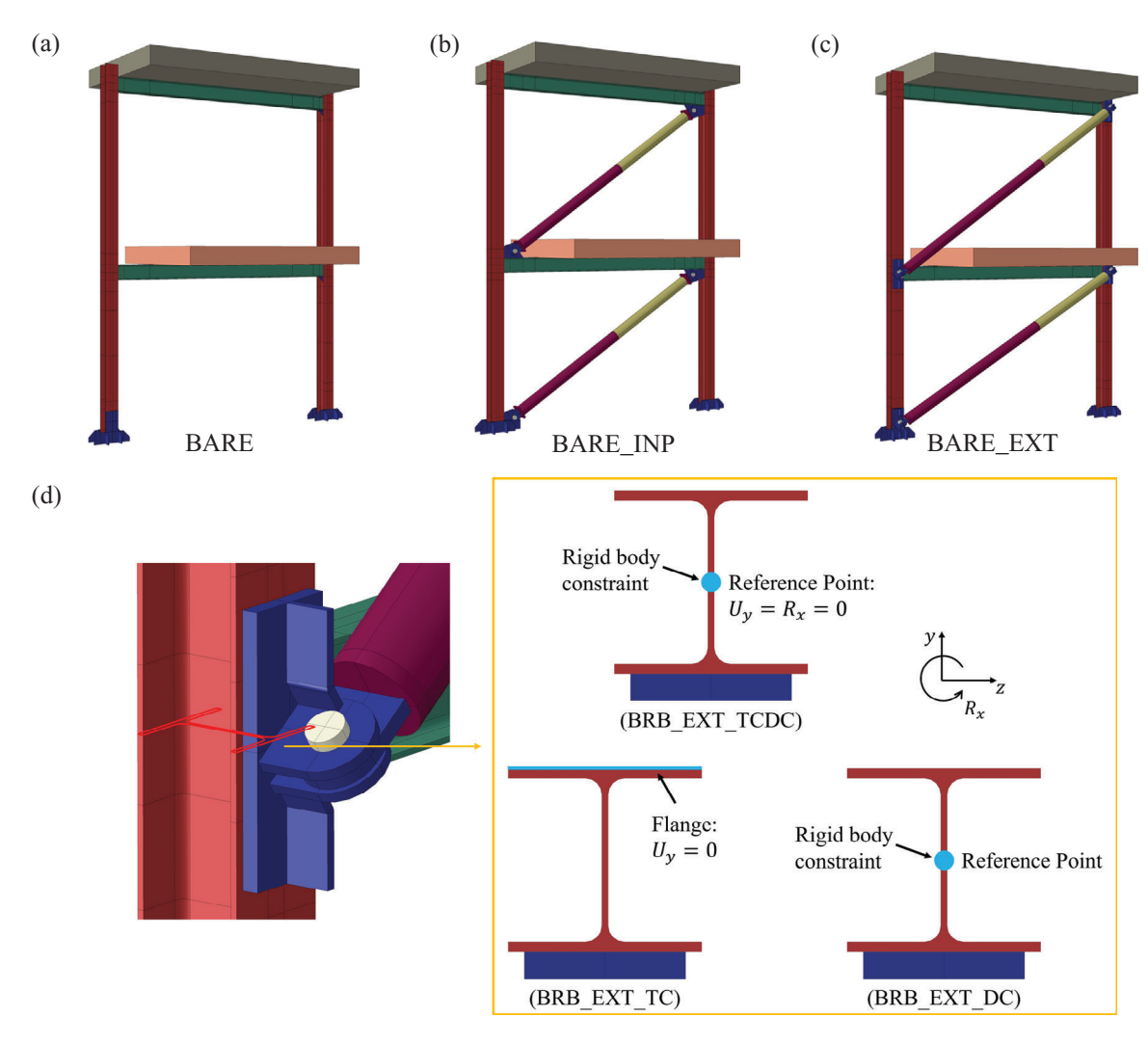


FIGURE 19 | FE models for the parametric analysis. (a) bare frame, (b) frame with in-plane BRBs, (c) frame with external BRBs, and (d) torsional (TC) and distortional (DC) constraints in the columns. BRBs, buckling-restrained braces.

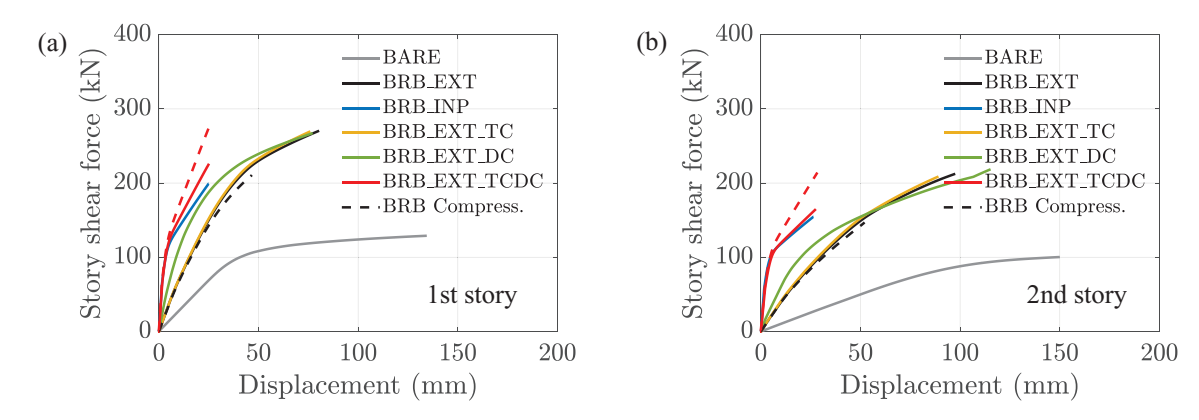


FIGURE 20 | Story shear versus inter-story drift curves. Comparisons of the BRB_EXT_TCDC, BRB_EXT_TC, and BRB_EXT_DC with the reference models: (a) first story; (b) second story (solid line represents BRB in tension, dash line represents BRBs in compression). BRB, buckling-restrained braces.

Nevertheless, this intervention did not significantly improve the frame's energy dissipation capacity, mainly because the BRBs were not adequately activated at lower displacements, as in the case of BRB_EXT_TCDC. Figure 20 shows the pushover curves with BRB in tension (solid lines). Additional pushover curves

representing BRB in compression were included (dash lines) for the models BRB_EXT and BRB_EXT_TCDC. Similar considerations can be drawn from those cases. It can be observed that the cases with BRB_EXT_show very similar results. Conversely, in the cases with BRB_EXT_TCDC the curve for the BRBs in

TABLE 8 | Additional torsional stiffness to the columns.

	Stiffness of the rotational spring (kNm)				
	1st story		2nd s	tory	
Coefficient α	Bottom Top		Bottom	Тор	
0.0	0.00	0.00	0.00	0.00	
0.5	27.80	2.67	2.67	1.26	
1.0	55.60	5.34	5.34	2.52	
2.5	139.00	13.34	13.34	6.30	
5.0	278.00	26.68	26.68	12.61	
10.0	555.99	53.37	53.37	25.22	
50.0	2779.96	266.83	266.83	126.10	
100.0	5559.93	533.65	533.65	252.19	
500.0	27799.64	2668.27	2668.27	1260.95	

compression shows a slightly higher hardening, reflecting the higher post-elastic response of the BRBs in compression.

In all cases, it can be observed that the pushover curves show a high post-yielding stiffness. On one end, this is due to the stiffness of the frame, which remains elastic, on the other end, to the stiffness of the BRBs, which accounts for the isotropic hardening, as discussed at the beginning of Section 4 and shown in Figure 18.

It is also noted that, by constraining the torsional and distortional deformability of columns in the connection zones, damage in the column (as shown in Figure 16) was effectively prevented, as no yielding or fracture was observed in columns. It is observed that the model BRB_EXT_TCDC shows a response similar to the model BRB_INP where the steel frame remained elastic for displacements within the capacity of BRBs.

4.2 | Parametric Analysis on the Torsional Stiffness of Column

The previous section highlighted that external BRBs could be effective solely if additional measures are implemented to increase the columns' torsional stiffness and prevent

> Story shear force (kN) 1st story 200 BRB_INP $\alpha = 5.0$ $\alpha = 0.0$ $\alpha = 10.0$ 100 $\alpha = 0.5$ $\alpha = 50.0$ $\alpha = 1.0$ $\alpha = 100.0$ $\alpha = 2.5$ $\alpha = 500.0$ 0 0 50 100 150 Displacement (mm)

flange-to-web distortional deformations. While preventing distortional deformations can be easily achieved through stiffening welded plates, increasing the torsional stiffness is a more difficult task and requires additional investigation.

A parametric analysis was conducted to investigate the influence of column torsional stiffness on the performance of retrofitted steel frames, provided that the distortional deformation of column flanges is prevented. To this end, additional eight FE models of the retrofitted steel frame were built based on the configuration of BRB_EXT_TCDC, in which the distortional deformation of the column flange was prevented at the controlled sections via the rigid body constraint, as shown in Figure 19. The additional torsional stiffness provided to the column was modeled through a rotational spring connecting each reference point and externally fixed. The stiffness values assigned to the springs were defined by evaluating the pure torsional stiffness of the column profile and amplifying them through coefficient α . The adopted values of the coefficient α are summarized in Table 8. The torsional stiffness of the column profile is computed as GJ/L_i , where GJ represents the torsional rigidity and L_i corresponds to the height of the BRB connections.

Figure 21 shows the results of the pushover analyses for all the models with increasing torsional stiffness in terms of shear story versus IDRs. The results show that by increasing the torsional stiffnesses, the frame's response approaches the limit case of in-plane BRBs (i.e., BRB_INP). The FE analyses showed the beneficial role of torsionally rigid columns (or the inclusion of torsional restraints), which allow exploiting the rigidity and ductility of the braces as well as reducing the flexural demand on the frame members.

This analysis allows for identifying the parameters affecting the torsional response experienced by the columns as a consequence of the use of BRB. A dimensionless parameter β was proposed, as defined in Equation (3), where F_y is the yield force of BRB, e represents the BRB eccentricity, K_t is the column torsional stiffness, that is, the sum of the torsional stiffness of the column, and the additional stiffness provided by the spring. In Equation (3), K_0 is the warping stiffness of the column cross-section, and GJ/L is the pure torsional rigidity of the column. The terms at the numerator represent the torsional moment applied to the column, while the terms at the denominator represent the torsional stiffness.

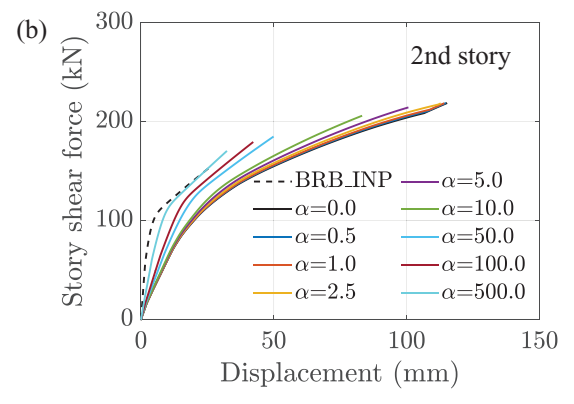


FIGURE 21 | Story shear versus inter-story drift curves. Comparisons between models with increasing torsional stiffness and the reference model with in-plane BRBs: (a) first story and (b) second story. BRB, buckling-restrained braces.

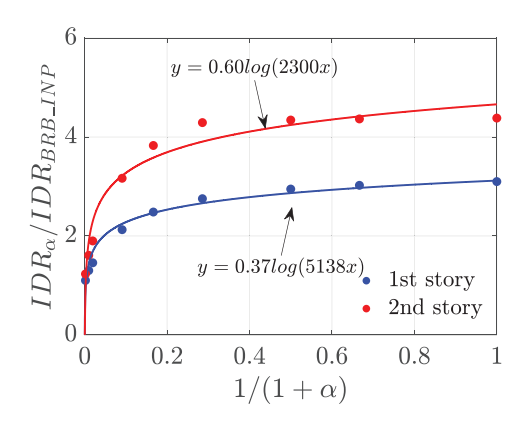


FIGURE 22 | Improvement of structural performance with external BRBs due to increasing column torsional stiffness (see Table 8 and Equation (3) for the definition of α). BRB, buckling-restrained braces.

Thus, a high β value indicates a more significant impact of BRB eccentricity.

$$\beta = \frac{F_y e}{K_t} = \frac{F_y e}{K_0 + \alpha \frac{GJ}{L_t}} \cong \frac{F_y e}{(1 + \alpha) \frac{GJ}{L_t}}$$
(3)

Based on the definition of β , several measures can be taken to reduce the impact of BRB eccentricity, such as selecting a BRB with low yield strength, minimizing the eccentricity of BRB connections, and/or increasing the column torsional stiffness. However, the former two are usually restricted by design requirements and geometric limitations and, hence, may not be easily achieved. Figure 22 illustrates the effectiveness of increasing column torsional stiffness to mitigate the impact of BRB eccentricity. The horizontal axis is related to $1/(1+\alpha)$, which represents the variable component of the parameter β that decreases by increasing the column torsional stiffness. In contrast, the vertical axis represents the IDRs normalized to the

IDRs of the BRB_INP model at the failure of BRBs. Figure 22 shows that the improvement in the structural performance is limited for $1/(1 + \alpha) > 0.25$ (i.e., $\alpha < 3$), and significant improvements are obtained starting from $1/(1 + \alpha) < \sim 0.1$ (i.e., $\alpha > \sim 10$).

5 | Local Retrofit of the BRB Connections

This section investigates the response of the structure with external BRBs by explicitly considering the contribution of transverse beams and slabs to the column torsional stiffness and the impact of stiffening welded plates to avoid distortion of the sections.

The BRB retrofitting was applied to the scaled structure introduced in Section 2 instead of the plane frame considered in the PsD test and the parametric analysis. Figure 23 shows the FE model of the 3D structure (denoted as BRB_EXT_PT), which was built following the same modeling strategies as the plane frame. To reduce the computational demand, only half the model was built, including appropriate boundary conditions at the end of the slab and transverse beams accounting for the symmetry of the structure. Stiffening plates were applied at the top, mid-height, and bottom of each BRB connection to avoid the distortion of the column flanges (Figure 23).

Figure 24 shows the comparisons between the response of BRB_EXT_PT and the reference models. The results show that the introduction of the stiffening plates and the slabs effectively prevents the columns from experiencing large torsional and distortional deformations. Figure 24a,b shows the results of the pushover analyses in terms of shear story versus IDRs, demonstrating that the performance of the BRB_EXT_PT is comparable to the model with in-plane BRBs. Additionally, Figure 24c,d shows that the IDRs corresponding to the failure of BRBs are less than 20% larger than those of the model with BRBs in-plane, indicating that the retrofit scheme using external BRBs with the

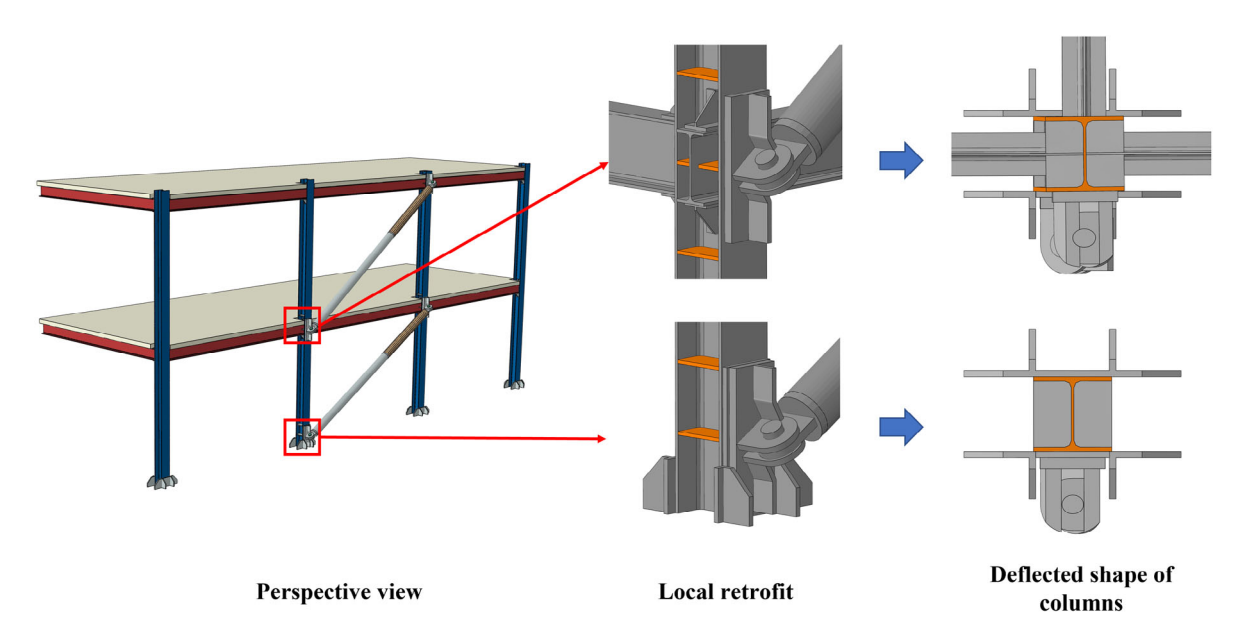
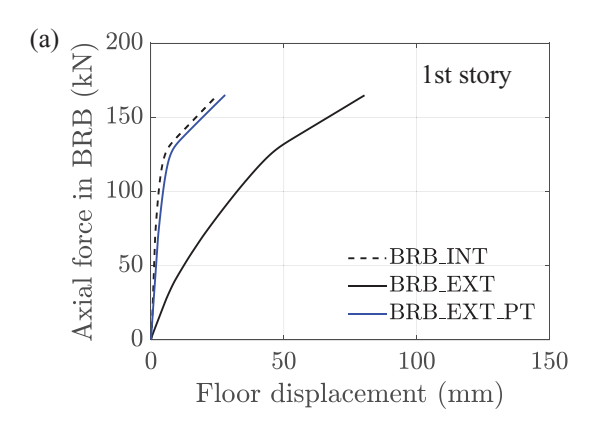


FIGURE 23 Perspective view of the Model BRB_EXT_PT, details of the local retrofit of BRB connections using stiffening plates and the deflected shape of columns at the mid-height of connections at the failure of BRBs. BRBs, buckling-restrained braces.



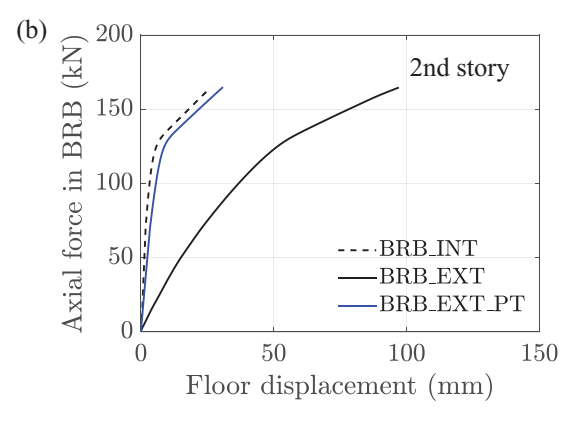


FIGURE 24 | BRBs axial forces. Comparisons of the pushover curves of Model BRB_EXT_PT with reference models: (a) first story and (b) second story. BRBs, buckling-restrained braces.

stiffening plates can lead to approximately the same structural performance as the conventional retrofit approach using internal BRBs.

6 | Conclusions

This paper investigates the seismic retrofitting of existing steel structures through buckling-restrained braces (BRBs) placed externally to the frame to minimize the invasiveness of the intervention. The paper presents the details of a large-scale PsD experimental campaign performed on a two-story steel MRF as part of the HITFRAMES (i.e., HybrId Testing of an Existing Steel Frame with Infills under Multiple EarthquakeS) SERA project. The frame was designed to be representative of existing (nonseismically designed) structures and was successively retrofitted with externally placed BRBs. The experimental results allowed the evaluation of the seismic response of the retrofitted structure, including the influence of the BRBs placement on the local and global response. The experimental results were essential for the calibration of advanced 3D FE models in ABAQUS. An extensive numerical parametric analysis was successively performed to investigate the influence of some key variables affecting the local and global response of the structure and to provide design recommendations. Based on the results of the study, the following conclusions are drawn:

- The eccentricity caused by the externally placed BRBs led to
 excessive torsional deformation of columns and distortional
 deformation of the flange where the BRB connections are
 located. For the present case study, this accounted for more
 than 80% reduction of lateral stiffness compared to the case of
 conventional in-plane placement of BRBs;
- The implementation of external BRBs without additional details to increase the stiffness of the connections could not adequately activate the BRB devices at low displacements; hence, it did not allow to achieve a performance comparable to conventional solutions with in-plane BRBs;
- The influence of the eccentricity of external BRBs can be reduced/removed, providing that sufficient constraints were applied to restrain the torsional and distortional deformation of columns simultaneously; however, restraining solely one

of the former two deformations would not lead to significant improvement of the structural performance;

- The parametric analysis showed that the relationship between
 the increase in torsional column stiffness and the reduction in
 interstory drift at BRB failure could be represented by a logarithmic regression. The key regression parameters are defined,
 offering some insights into the key parameters controlling the
 response;
- For the present case study structure, the parametric analysis showed that providing that the distortional deformation of flanges was prevented, the column torsional stiffness at the joint location should be at least ten times larger to effectively improve the seismic performance to a level that is comparable with the case of in-plane BRBs;
- The more comprehensive FE model, also including the presence of adjacent bays, transverse beams, and concrete slab, demonstrated that stiffening plates could be used to prevent the distortional deformations of the section. On the other side, ensuring proper interactions of the column with the adjacent beams and concrete slab can provide the required torsional stiffness. The numerical simulations demonstrated that the careful design of local measures at the connection represents a potential solution to address the detrimental effects related to the BRBs eccentricity. The results showed that the proposed solution can lead to a performance comparable to conventional retrofit strategies with in-plane BRBs.

The obtained results, from one side, underline the importance of carefully designing the BRBs' connection and the impact it can have on the global response of the frame; on the other side, they provide important design recommendations for innovative retrofit solutions with significant benefits in terms of increased seismic performance and reduced business interruption during the retrofitting operations.

The results of this study are limited to the considered configuration. Additional studies should be carried out to investigate, numerically and experimentally, different structures, BRBs' properties, and configurations to generalize the results. The proposed/identified solution to avoid torsional and distortional

deformations was investigated only through numerical simulations in ABAQUS. Although these models have been validated against experimental results, additional tests to validate this strategy would be beneficial. Moreover, the obtained results provide several insights into the design of the proposed solution, but clear guidelines are still missing. Further studies are deemed necessary to ensure the adequate performance of externally placed BRBs.

Acknowledgments

The financial support from the Seismic Engineering Research Infrastructure (SERA) for the "HybrId Testing of an Existing Steel Frame with Infills under Multiple Earthquakes" (HITFRAMES) SERA Project, funded within the H2020-INFRAIA-2016-2017 Framework Program of the European Commission under grant agreement No. 730900, is greatly appreciated. Any opinions, findings, conclusions, or recommendations expressed in this paper are those of the Authors and do not necessarily reflect those of SERA sponsors.

Data Availability Statement

The data that support the findings of this study are available from the corresponding author upon reasonable request.

References

- 1. Federal Emergency Management Agency (FEMA), State of the Art Report on Past Performance of Steel Moment-frame Buildings in Earthquakes (FEMA, Washington, DC, 2000).
- 2. L. Di Sarno, F. Paolacci, and A. G. Sextos, "Seismic Performance Assessment of Existing Steel Buildings: A Case Study," *Key Engineering Materials* 763 (2018): 1067–1076.
- 3. L. Di Sarno and J. R. Wu, "Seismic Assessment of Existing Steel Frames With Masonry Infills," *Journal of Constructional Steel Research* 169 (2020): 106040, https://doi.org/10.1016/j.jcsr.2020.106040.
- 4. L. F. Gutiérrez-Urzúa, F. Freddi, and L. Di Sarno, "Comparative Analysis of Code Based Approaches for the Seismic Assessment of Existing Steel Moment Resisting Frames," *Journal of Constructional Steel Research* 181 (2021): 106589, https://doi.org/10.1016/j.jcsr.2021.106589.
- 5. European Committee for Standardization (CEN), Eurocode 8: Design of Structures for Earthquake Resistance—Part 3: Assessment and Retrofitting of Buildings (CEN, Brussels, Belgium, 2005).
- 6. American Institute of Steel Construction (AISC), Seismic Provisions for Structural Steel Buildings, ANSI/AISC 341-16, ANSI/AISC 341-16. (AISC, Chicago, IL, 2016).
- 7. F. Freddi, C. Galasso, G. Cremen, et al., "Innovations in Earthquake Risk Reduction for Resilience: Recent Advances and Challenges," *International Journal of Disaster Risk Reduction* 60 (2021): 102267, https://doi.org/10.1016/j.ijdrr.2021.102267.
- 8. T. T. Soong and B. F. Spencer, "Supplemental Energy Dissipation: State-of-the-Art and State-of-the-Practice," *Engineering Structures* 24, no. 3 (2002): 243–259, https://doi.org/10.1016/S0141-0296(01)00092-X.
- 9. Q. Xie, "State of the Art of Buckling-Restrained Braces in Asia," *Journal of Constructional Steel Research* 61, no. 6 (2005): 727–748.
- 10. R. Tremblay, P. Bolduc, R. Neville, and R. DeVall, "Seismic Testing and Performance of Buckling-restrained Bracing Systems," *Canadian Journal of Civil Engineering* 33, no. 2 (2006): 183–198.
- 11. A. Zona and A. Dall'Asta, "Elastoplastic Model for Steel Buckling-Restrained Braces," *Journal of Constructional Steel Research* 68, no. 1 (2012): 118–125.
- 12. L. Di Sarno and G. Manfredi, "Experimental Tests on Full-Scale RC Unretrofitted Frame and Retrofitted With Buckling-Restrained Braces,"

- Earthquake Engineering and Structural Dynamics 41, no. 2 (2012): 315–333, https://doi.org/10.1002/eqe.1131.
- 13. G. Della Corte, M. D'Aniello, and R. Landolfo, "Field Testing of All-Steel Buckling-Restrained Braces Applied to a Damaged Reinforced Concrete Building," *Journal of Structural Engineering (United States)* 141, no. 1 (2015): D4014004, https://doi.org/10.1061/(ASCE)ST.1943-541X. 0001080
- 14. A.-C. Wu, K.-C. Tsai, H.-H. Yang, et al., "Hybrid Experimental Performance of a Full-Scale Two-Story Buckling-Restrained Braced RC Frame," *Earthquake Engineering and Structural Dynamics* 46, no. 8 (2017): 1223–1244, https://doi.org/10.1002/eqe.2853.
- 15. R. Ozcelik and E. F. Erdil, "Pseudodynamic Test of a Deficient RC Frame Strengthened With Buckling Restrained Braces," *Earthquake Spectra* 35, no. 3 (2019): 1163–1187, https://doi.org/10.1193/122317EQS26.
- 16. Y. Qie, F. Barbagallo, E. Marino, C. Du, and T. Wang, "Full-Scale Hybrid Test for Realistic Verification of a Seismic Upgrading Technique of RC Frames by BRBs," *Earthquake Engineering and Structural Dynamics* 49, no. 14 (2020): 1452–14721, https://doi.org/10.1002/eqe.3312.
- 17. L. A. Fahnestock, J. M. Ricles, and R. Sause, "Experimental Evaluation of a Large-Scale Buckling-Restrained Braced Frame," *Journal of Structural Engineering* 133, no. 9 (2007): 1205–1214, https://doi.org/10.1061/(ASCE)0733-9445(2007)133:9(1205).
- 18. P. C. Lin, K. C. Tsai, K. J. Wang, et al., "Seismic Design and Hybrid Tests of a Full-Scale Three-Story Buckling-Restrained Braced Frame Using Welded End Connections and Thin Profile," *Earthquake Engineering and Structural Dynamics* 41, no. 5 (2012): 1001–1020, https://doi.org/10.1002/eqe.1171.
- 19. K. D. Palmer, C. W. Roeder, D. E. Lehman, T. Okazaki, and C. Shield, "Experimental Performance of Steel Braced Frames Subjected to Bidirectional Loading," *Journal of Structural Engineering* 139, no. 8 (2013): 1274–1284, https://doi.org/10.1061/(ASCE)ST.1943-541X.0000624.
- 20. H. H. Khoo, K. C. Tsai, C. Y. Tsai, C. Y. Tsai, and K. J. Wang, "Bidirectional Substructure Pseudo-Dynamic Tests and Analysis of a Full-Scale Two-Story Buckling-Restrained Braced Frame," *Earthquake Engineering and Structural Dynamics* 45, no. 7 (2016): 1085–1107, https://doi.org/10.1002/eqe.2696.
- 21. C. C. Chou, C. H. Hsiao, Z. B. Chen, P. T. Chung, and D. H. Pham, "Seismic Loading Tests of Full-Scale Two-Story Steel Building Frames With Self-Centering Braces and Buckling-Restrained Braces," *Thin-Walled Structure* 140 (2019): 168–181, https://doi.org/10.1016/j.tws. 2019.03.024.
- 22. S. Mojiri, P. Mortazavi, O.-S. Kwon, and C. Christopoulos, "Seismic Response Evaluation of a Five-Story Buckling-Restrained Braced Frame Using Multi-Element Pseudo-Dynamic Hybrid Simulations," *Earthquake Engineering and Structural Dynamics* 50, no. 12 (2021): 3243–326510, https://doi.org/10.1002/eqe.3508.
- 23. L. Di Sarno and A. Elnashai, "Bracing Systems for Seismic Retrofitting of Steel Frames," *Journal of Constructional Steel Research* 65, no. 2 (2009): 452–465, https://doi.org/10.1016/j.jcsr.2008.02.013.
- 24. L. Di Sarno and G. Manfredi, "Seismic Retrofitting With Buckling Restrained Braces: Application to an Existing Non-Ductile RC Framed Building," *Soil Dynamics and Earthquake Engineering* 30, no. 11 (2010): 1279–1297, https://doi.org/10.1016/j.soildyn.2010.06.001.
- 25. E. M. Güneyisi, "Seismic Reliability of Steel Moment Resisting Framed Buildings Retrofitted With Buckling Restrained Braces," *Earthquake Engineering and Structural Dynamics* 41, no. 5 (2012): 853–874, https://doi.org/10.1002/eqe.1161.
- 26. F. Freddi, E. Tubaldi, L. Ragni, and A. Dall'Asta, "Probabilistic Performance Assessment of Low-Ductility Reinforced Concrete Frames Retrofitted With Dissipative Braces," *Earthquake Engineering and Structural Dynamics* 42, no. 7 (2013): 993–1011, https://doi.org/10.1002/eqe. 2255.
- 27. F. Freddi, E. Tubaldi, A. Zona, and A. Dall'Asta, "Seismic Performance of Dual Systems Coupling Moment-Resisting and Buckling-Restrained

- Braced Frames," *Earthquake Engineering and Structural Dynamics* 50, no. 2 (2021): 329–353, https://doi.org/10.1002/eqe.3332.
- 28. F. Freddi, J. Ghosh, N. Kotoky, and M. Raghunandan, "Device Uncertainty Propagation in Low-Ductility RC Frames Retrofitted With BRBs for Seismic Risk Mitigation," *Earthquake Engineering and Structural Dynamics* 50, no. 9 (2021): 2488–2509, https://doi.org/10.1002/eqe.3456.
- 29. P. Castaldo, E. Tubaldi, F. Selvi, and L Gioiella, "Seismic Performance of an Existing RC Structure Retrofitted With Buckling Restrained Braces," *Journal of Building Engineering* 33 (2021): 101688, https://doi.org/10.1016/j.jobe.2020.101688.
- 30. L. F. Gutiérrez-Urzúa and F. Freddi, "Influence of the Design Objectives on the Seismic Performance of Steel Moment Resisting Frames Retrofitted With Buckling Restrained Braces," *Earthquake Engineering and Structural Dynamics* 51, no. 13 (2022): 3131–3153, https://doi.org/10.1002/eqe.3717.
- 31. R. Chelapramkandy, J. Ghosh, and F. Freddi, "Influence of Masonry Infills on Seismic Performance of BRB-Retrofitted Low-Ductile RC Frames," *Earthquake Engineering and Structural Dynamics* (2024), http://doi.org/10.1002/eqe.4255.
- 32. A. Dall'Asta, L. Ragni, E. Tubaldi, and F Freddi, "Design Methods for Existing RC Frames Equipped With Elasto-Plastic or Viscoelastic Dissipative Braces," in *Proceedings of XIII Convegno Nazionale* ANIDIS (Bologna, Italy, 2009).
- 33. D. R. Sahoo and S.-H. Chao, "Performance-Based Plastic Design Method for Buckling-Restrained Braced Frames," *Engineering Structures* 32, no. 9 (2010): 2950–2958, https://doi.org/10.1016/j.engstruct.2010.05. 014.
- 34. L. Ragni, A. Zona, and A. Dall'Asta, "Analytical Expressions for Preliminary Design of Dissipative Bracing Systems in Steel Frames," *Journal of Constructional Steel Research* 67, no. 1 (2011): 102–113, https://doi.org/10.1016/j.jcsr.2010.07.006.
- 35. F. Sutcu, T. Takeuchi, and R. Matsui, "Seismic Retrofit Design Method for RC Buildings Using Buckling-Restrained Braces and Steel Frames," *Journal of Constructional Steel Research* 101 (2014): 304–313, https://doi.org/10.1016/j.jcsr.2014.05.023.
- 36. F. Barbagallo, M. Bosco, E. M. Marino, P. P. Rossi, and P. R. Stramondo, "A Multi-Performance Design Method for Seismic Upgrading of Existing RC Frames by BRBs," *Earthquake Engineering and Structural Dynamics* 46, no. 7 (2016): 1099–1119, https://doi.org/10.1002/eqe.2846.
- 37. G. Di Lorenzo, E. Colacurcio, A. Di Filippo, A. Formisano, A. Massimilla, and R. Landolfo, "State-of-the-Art on Steel Exoskeletons for Seismic Retrofit of Existing RC Buildings," *Ing Sismica* 37, no. 1 (2020): 33–50.
- 38. C. Passoni, J. Guo, C. Christopoulos, A. Marini, and P. Riva, "Design of Dissipative and Elastic High-Strength Exoskeleton Solutions for Sustainable Seismic Upgrades of Existing RC Buildings," *Engineering Structures* 221 (2020): 111057, https://doi.org/10.1016/j.engstruct.2020.111057.
- 39. G. Di Lorenzo, R. Tartaglia, A. Prota, and R. Landolfo, "Design Procedure for Orthogonal Steel Exoskeleton Structures for Seismic Strengthening," *Engineering Structures* 275 (2023): 115252, https://doi.org/10.1016/j.engstruct.2022.115252.
- 40. T. Kikuchi, T. Takeuchi, S. Fujimori, and A. Wada, "Design of Seismic Isolated Tall Building With High Aspect-Ratio," *International Journal of High-Rise Buildings* 3, no. 1 (2014): 1–8.
- 41. T. Takeuchi, K. Yasuda, and M. Iwata, Seismic Retrofitting Using Energy Dissipation Façades (San Francisco: ATC-SEI09, 2009): 12.
- 42. R. L. Brockenbrough and J. Schuster, *Design Guide 15: Rehabilitation and Retrofit*, 2nd edition (American Institute of Steel Construction, Chicago, IL, 2018).
- 43. European Committee for Standardization (CEN). Eurocode 8: Design of Structures for Earthquake Resistance—Part 1: General Rules, Seismic Actions and Rules for Buildings (CEN, Brussels, Belgium, 2004).

- 44. L. Di Sarno, F. Freddi, and M. D'Aniello, "Assessment of Existing Steel Frames: Numerical Study, Pseudo-Dynamic Testing and Influence of Masonry Infills," *Journal of Constructional Steel Research* 185 (2021): 106873, https://doi.org/10.1016/j.jcsr.2021.106873.
- 45. F. McKenna, M. H. Scott, and G. L. Fenves, "Non-Linear Finite-Element Analysis Software Architecture Using Object Composition," *Journal of Computing in Civil Engineering* 24 (2010): 95–107, https://doi.org/10.1061/(ASCE)CP.1943-5487.0000002.
- 46. Dassault Systèmes, ABAQUS/Standard User's Guide, Version 6 14 (SIMULIA, Providence, RI, 2014).
- 47. European Committee for Standardization (CEN), Eurocode 3: Design of Steel Structures—Part 1-1: General Rules and Rules for Buildings (CEN, Brussels, Belgium, 2011).
- 48. European Committee for Standardization (CEN), Eurocode 3: Design of Steel Structures—Part 1–8: Design of Joints (CEN, Brussels, Belgium, 2005).
- 49. International Organization for Standardization (ISO), ISO 6892-1:2019 Metallic Materials—Tensile Testing—Part 1: Method of Test at Room Temperature (ISO, Geneva, Switzerland, 2019).
- 50. S. Bousias, L. Di Sarno, F. Freddi, et al., "Hybrid simulation of existing steel frames with external BRBs for seismic retrofitting (Project SERA-HITFRAMES_Part 2) [Data set]," Zenodo (2024), https://doi.org/10.5281/ZENODO.10843919.
- 51. L. Luzi, R. Puglia, E. Russo, et al., "The Engineering Strong—Motion Database: A Platform to Access Pan-European Accelerometric Data," *Seismological Research Letters* 87, no. 4 (2016): 987–997.
- 52. D. Combescure and P. Pegon, "α-Operator Splitting Time Integration Technique for Pseudodynamic Testing Error Propagation Analysis," *Soil Dynamics and Earthquake Engineering* 16, no. 7–8 (1997): 427–443.
- 53. X. Huang and O.-S. Kwon, "A Generalized Numerical/Experimental Distributed Simulation Framework," *Journal of Earthquake Engineering* 24, no. 4 (2018): 682–703.
- 54. X. Huang, J. Park, and O.-S. Kwon, "Network Interface Program for Actuator Controllers for Pseudo-Dynamic Hybrid Simulation," *Journal of Earthquake Engineering* 28, no. 1 (2023): 266–287.
- 55. O.-S. Kwon and V. Kammula, "Model Updating Method for Substructure Pseudo-Dynamic Hybrid Simulation," *Earthquake Engineering and Structural Dynamics* 42, no. 13 (2013): 1971–1984, https://doi.org/10.1002/eqe.2307.
- 56. C. Y. Tsai, K. C. Tsai, L. W. Chen, and A. C. Wu, "Seismic Performance Analysis of BRBs and Gussets in a Full-Scale 2-Story BRB-RCF Specimen," *Earthquake Engineering and Structural Dynamics* 47, no. 12 (2018): 2366–2389, https://doi.org/10.1002/eqe.3073.